

# **Modeling and Monitoring of Otolith Organ Performance in U.S. Navy Operating Environments**

Elizabeth Ferreira McGrath

Submitted to the Faculty of the Virginia Polytechnic Institute and State University in partial fulfillment of  
the requirements for the degree of

Doctor of Philosophy

in

Engineering Mechanics

J. Wallace Grant, Chair  
Daniel J. Inman  
Bradley G. Klein  
Ronald D. Kriz  
Brian J. Love

Blacksburg, VA

Keywords: finite element, otolith, eye movement, vestibular model

Copyright 2003, Elizabeth Ferreira McGrath

# Modeling and Monitoring of Otolith Organ Performance in U.S. Navy Operating Environments

Elizabeth Ferreira McGrath

## *(ABSTRACT)*

Previous mathematical modeling work has produced a transfer function that relates otoconial layer displacement to stimulus acceleration. Due to the complexity of this transfer function, time domain solutions may be obtained only through numerical methods. In the current work, several approximations are introduced to the transfer function that result in its simplification. This simplified version can be inverted to yield analytic time domain solutions. Results from a frequency response analysis of the simplified transfer function are compared with the same results from the complete transfer function, and with mammalian first-order neuron frequency response data. There is good agreement in the comparisons. Time domain solutions of the approximation are compared to numerical solutions of the full transfer function, and again there is a good match. System time constants are calculated from the simplified transfer function.

A 2-D finite element model of a mammalian utricular macula is presented. Physical dimensions used in the model are taken from mammalian anatomical studies. Values for the material properties of the problem are not readily available; however, ranges are chosen to produce realistic physiologic behavior. Deflections predicted by this model show that a single value for hair bundle stiffness throughout the organ is inadequate for the organ to respond to the entire range of human acceleration perception. Therefore, it is necessary for a range of hair bundle stiffnesses to exist in each organ. Natural frequencies calculated in this model support previous studies on vestibular damage due to low frequency sound.

Divers exposed to high-intensity underwater sound have experienced symptoms attributed to vestibular stimulation. An in-water video-oculography (VOG) system was developed to monitor divers' eye movements, particularly torsional, during exposure to varying underwater sound signals. The system included an underwater closed-circuit video camera with infrared lights attached to the diver's mask with an adjustable mounting bracket. The video image was sent to a surface control room for real-time and post-experiment processing. Six divers at 60 feet in open water received 15 minutes daily cumulative exposure of 240-320 Hertz underwater sound at 160 dB re 1  $\mu$ Pa for 10 days. No spontaneous primary position nystagmus, horizontal, vertical or torsional, was detected in any diver. This experiment was the first successful attempt to record and analyze eye movements underwater.

## ***ACKNOWLEDGEMENTS***

This work would not have been possible without the generous support of CAPT Angus Rupert, MC USN of the Naval Aerospace Medical Research Laboratory in Pensacola, FL. I would like to offer him my sincere thanks for providing me with this opportunity.

Without the guidance, encouragement, and patience (nearly 10 years worth), of my advisor, Dr. Wally Grant, this work would definitely not have seen its completion. A huge thank you, Dr. G, for not giving up on me!

When I came to Pensacola in 1995 to do research for this dissertation with Dr. Grant, who was here on sabbatical for a year at the time, he was somewhat apprehensive about having me come, for fear I might be distracted by the naval aviators. Well, his worst fears were realized when I did in fact meet my soulmate and proceed to put the dissertation work on the back burner in favor of marriage and a family. So, Dr. Grant, I apologize for making you wait this long for the dissertation, but thank you for introducing me to my husband!

Thanks to my family for being so supportive. My wonderful husband, who by the way is not a naval aviator, has been there to help me at every turn. Thank you, Brad, I couldn't have done it without you! Thanks to my parents for their support and all that babysitting. And finally, thanks to my beautiful children just for being. They put it all in perspective.

**This research was sponsored by the Office of Naval Research under work unit  
61153N.MR04101.00F-7303.**

The views expressed in this document are those of the author and do not necessarily reflect the official policy or position of the Department of the Navy, Department of Defense, nor the U.S. Government.

# **TABLE OF CONTENTS**

<b>INTRODUCTION.....</b>	<b>1</b>
1.1    OPENING REMARKS .....	1
1.2    VESTIBULAR SYSTEM .....	2
1.3    THESIS GOALS .....	7
1.4    THESIS ORGANIZATION .....	8
<b>A SIMPLIFIED MATHEMATICAL MODEL TO PREDICT OTOLITH MEMBRANE DISPLACEMENT.....</b>	<b>10</b>
2.1    PREVIOUS MATHEMATICAL MODELS .....	10
2.2    SIMPLIFYING A COMPLEX TRANSFER FUNCTION .....	16
2.3    THE SIMPLIFIED MODEL .....	21
2.4    A PHYSICAL SIMPLIFICATION .....	26
2.5    DIMENSIONAL FORM OF THE APPROXIMATE TRANSFER FUNCTION .....	29
2.6    TIME DOMAIN SOLUTIONS.....	32
2.7    DISCUSSION AND CONCLUSIONS .....	38
<b>A TWO-DIMENSIONAL FINITE ELEMENT MODEL FOR ANALYSIS OF OTOLITH ORGAN DEFORMATION .....</b>	<b>42</b>
3.1    INTRODUCTION.....	42
3.2    BACKGROUND.....	44
3.2.1    Finite Element Modeling .....	44
3.2.2    Otolith Organ Morphology.....	46
3.2.3    Displacement of Otolithic Membranes Deflects Hair Bundles.....	50
3.2.4    Ciliary Bundle Deflection Initiates a Neural Signal.....	52
3.3    THE MODEL .....	54
3.3.1    Finite Element Representation of Otolithic Organs .....	54
3.3.2    Assigning Material Properties.....	58
3.3.3    Boundary Conditions.....	60
3.4    RESULTS.....	60
3.4.1    Results for Deformation Due to Acceleration .....	60
3.4.2    Results for Variation in Hair Bundle Stiffness .....	62
3.4.3    Natural Frequencies and Mode Shapes.....	64
3.5    CONCLUSIONS .....	66
<b>AN UNDERWATER VIDEO-OCULOGRAPHY SYSTEM TO MONITOR VESTIBULAR OUTPUT .....</b>	<b>68</b>
4.1    BACKGROUND.....	68
4.2    MATERIALS AND METHODS .....	71
4.2.1    Equipment.....	71
4.2.2    Subjects.....	76
4.2.3    Procedure .....	77
4.3    RESULTS.....	79
4.4    DISCUSSION .....	83
4.5    CONCLUSIONS .....	85
<b>CONCLUDING REMARKS.....</b>	<b>86</b>
<b>REFERENCES .....</b>	<b>90</b>
<b>VITA.....</b>	<b>100</b>

# FIGURES

Figure 1.1 – The membranous labyrinth of the inner ear. From a 3-D reconstruction of a gerbil MRI scan (reproduced with permission from Henson 2000).....	3
Figure 1.2 – Schematic of the horizontal semicircular canal and utricle. ....	4
Figure 1.3 – Cross-section of an otolithic organ. ....	5
Figure 2.1 – Free-body force diagrams of the otoconial layer, endolymph fluid layer, and gel layer. The interfaces are coupled by shear stresses of equal magnitude that act in opposite directions on each surface. The forces acting at these interfaces are the product of shear stress, $\tau$ , and area, $dA$ . The $B_x$ and $W_x$ forces are the components of the buoyant and weight forces acting in the plane of the otoconial layer. $\hat{V}_s$ is the skull velocity. ....	12
Figure 2.2 – Frequency response diagram of the complete transfer function compared with approximations where the coth term is replaced with one, two, or three terms of a Taylor series expansion. In this comparison the $\sqrt{s}$ term is retained in full so that only the effects of the coth approximations are evaluated. Values for the nondimensional variables for the comparisons are $R=0.5$ , $\epsilon=0.2$ , and $M=10$ . The single-term approximation is chosen for use in the simplified transfer function. The two-term approximation is almost an exact match, however, the one-term approximation is good and less complex. By choosing the less complex single-term approximation, the resulting transfer function is simplified; and, the time response results are as good as with the more complex two-term approximation. ....	18
Figure 2.3 – Frequency response diagram of the complete transfer function compared with approximations where the $\sqrt{s}$ term is replaced with one, two, or three terms of a Taylor series expansion. In this comparison the coth term is retained in full so that only the effects of the $\sqrt{s}$ approximations are evaluated. Values for the nondimensional variables for the comparisons are $R=0.5$ , $\epsilon=0.2$ , and $M=10$ . The two-term approximation is chosen for use in the simplified transfer function. The two-term approximation is a good match over the entire frequency range and proves to be a much better match in the time domain solutions than either the one-term or three-term approximations. ....	20
Figure 2.4 – Frequency response diagram of the complete transfer function compared with the final version of the approximate transfer function showing the effects of the nondimensional variable $M$ . Here $M$ is varied over its likely range, 1 – 20, while $\epsilon$ and $R$ are held constant at 0.2 and 0.5, respectively. ....	22
Figure 2.5 – Frequency response diagram of the complete transfer function compared with the final version of the approximate transfer function showing the effects of the nondimensional variable $R$ . Here $R$ is varied over its likely range, 0.25 – 0.75, while $\epsilon$ and $M$ are held constant at 0.2 and 10, respectively. ....	23
Figure 2.6 – Frequency response diagram of the complete transfer function compared with the final version of the approximate transfer function showing the effects of the nondimensional variable $\epsilon$ . Here $\epsilon$ is varied over its likely range, 0.01 – 1, while $R$ and $M$ are held constant at 0.5 and 10, respectively. ....	24
Figure 2.7 – Frequency response of the simplified transfer function, Equation 2.18, compared to experimental data from Goldberg et al. (1990). The simplified transfer function curve was fit to the utricular neural afferent data by using a regression analysis where $\epsilon$ and $M$ were allowed to vary, and $R$ was held constant. The magnitude of the experimental data had been normalized, and the simplified transfer function curve was shifted upward to match the experimental data. This shifting was accomplished by matching the flat response portion of the curve to the average of the middle four data points, which produced a simple shifting upward. The phase curve was unchanged. The low-frequency amplitude attenuation and phase lead of the physiologic data are probably due to nonmechanical effects. ....	25
Figure 2.8 – Time domain solutions of the complete transfer function and the approximate transfer function for a step change in skull velocity of magnitude one. The effects of varying $\epsilon$ are shown over the range $\epsilon=0.2$ to $\epsilon=2.0$ . The nondimensional variables $R$ and $M$ are held constant at 0.75 and 10 respectively. The complete transfer function was solved using a finite difference technique, while the approximate transfer function was solved using Matlab. For real time comparisons, 1 nondimensional time unit = 0.529 msec, where the following values were used for conversion: $\mu_f=0.85\text{mPa sec}$ , $\rho_0=2.0\text{ kg/m}^3$ , $b=15\mu\text{m}$ . ....	33

Figure 2.9 – Time domain solutions of the complete transfer function and the approximate transfer function for a step change in skull velocity of magnitude one. The effects of varying $R$ are shown over the range $R=0.25$ to $R=0.75$ . The nondimensional variables $\varepsilon$ and $M$ are held constant at 0.2 and 10 respectively. The complete transfer function was solved using a finite difference technique, while the approximate transfer function was solved using Matlab. For real time comparisons, 1 nondimensional time unit = 0.529 msec, where the following values were used for conversion: $\mu_f=0.85\text{mPa sec}$ , $\rho_0=2.0\text{ kg/m}^3$ , $b=15\mu\text{m}$ .	34
Figure 2.10 – Time domain solutions of the complete transfer function and the approximate transfer function for a step change in skull velocity of magnitude one. The effects of varying $M$ are shown over the range $M=1$ to $M=20$ . The nondimensional variables $R$ and $\varepsilon$ are held constant at 0.75 and 0.2 respectively. The complete transfer function was solved using a finite difference technique, while the approximate transfer function was solved using Matlab. For real time comparisons, 1 nondimensional time unit = 0.529 msec, where the following values were used for conversion: $\mu_f=0.85\text{mPa sec}$ , $\rho_0=2.0\text{ kg/m}^3$ , $b=15\mu\text{m}$ .	35
Figure 2.11 – Solution for a step change in skull velocity (acceleration impulse) over a long time period. Here, the trend for the otoconial layer displacement to return to zero can be seen. The system damping, represented by $M$ , affects the magnitude of the initial displacement and the time it takes for the otoconial layer to return to zero displacement. For real time comparisons 100 nondimensional time units= 52.9 msec, where the following values were used for conversion: $\mu_f=0.85\text{ mPa sec}$ , $\rho_0=2.0\text{ kg/m}^3$ , $b=15\mu\text{m}$ .	36
Figure 2.12 – Solution for a step change in skull acceleration of magnitude 1. The system damping, represented by $M$ , influences the time it takes for maximum displacement to be reached. For real time comparisons 100 nondimensional time units= 52.9 msec, where the following values were used for conversion: $\mu_f=0.85\text{ mPa sec}$ , $\rho_0=2.0\text{ kg/m}^3$ , $b=15\mu\text{m}$ .	37
Figure 3.1 - Section of an otolith organ showing its layered structure.	47
Figure 3.2 - Topographic study of a guinea pig right utricular macula showing its cupped nature. The axes are parallel to the stereotaxic coordinate axes since the data points were gathered in the guinea pig stereotaxic coordinate system. (from Curthoys 1996).	48
Figure 3.3 - Turtle utricular macula showing striolar, medial, and lateral zones. The otoconial and gel layers have been removed, exposing the neuroepithelium and hair cell ciliary bundles (from Peterson 1996).	50
Figure 3.4 – Otoconial layer displacement due to acceleration.	51
Figure 3.5 – Hair cell depolarization versus ciliary bundle deflection (Reprinted from Howard and Hudspeth 1988, with permission from Elsevier).	52
Table 3.1 - Different hair cell bundle stiffness values.	53
Figure 3.6 – Scanning micrograph showing variations in hair bundle morphology on the macula utriculi of the chinchilla (magnification 4650). Note the shorter stereocilia of the two bundles marked by arrows, which may contribute to morphologic stiffness variations. (from Lindeman et al., 1970).	54
Figure 3.7 – A high magnification photo of a section through a macula sacculi from a squirrel monkey. The schematic defines the layers and their dimensions. The cupular and subcupular zones are the gel and gel meshwork layers respectively (from Igarashi, 1966).	55
Figure 3.8 - Finite element representation of a section through a mammalian utricular macula.	56
Figure 3.9 – (a)Contour plot showing otolith organ deformation under a 1g load. (b)Graph showing variation in bundle tip deflection over the surface of the sensory epithelium.	61
Figure 3.10 - Range of human acceleration perception and the necessary bundle stiffness variation predicted by the model to accommodate this range (hair bundle stiffness, $k$ , is $\times 10^{-4}\text{ N/m}$ ).	62
Figure 3.11 – Model configured with hair cell bundles of alternating stiffness values (the units for $k$ are $\text{N/m}$ ). In case a). a 0.5g load is sensed by the less stiff bundles while the stiffer bundles are undeflected. In case b). a 5g load saturates the less stiff bundles while being sensed by the stiffer bundles.	63
Figure 3.12 – Results of the natural frequency analysis. The model is shown in its deformed state for the first four modes of oscillation.	65
Figure 4.1 – Full-face diving mask with video-oculography camera mounted over right eye.	72
Figure 4.2 – Fully enclosed diving helmet with video-oculography camera mounted over right eye.	73
Figure 4.3 – Control room set-up.	74
Figure 4.4 – Sound field test set-up (from NSMRL, 1995).	75

<i>Figure 4.5 – Subject wearing full-face mask with eye camera entering test area.....</i>	<i>76</i>
<i>Figure 4. 6 – Diver in test position (from NSMRL, 1995).....</i>	<i>78</i>
<i>Figure 4.7 – Digitized eye image during torsional nystagmus analysis. ....</i>	<i>80</i>
<i>Figure 4.8 – Graph of eye torsion angle versus time during the head tilt portion of the dive. ....</i>	<i>81</i>
<i>Figure 4.9 – Graph of eye torsion angle versus time during the sound exposure portion of the dive .....</i>	<i>82</i>

# ***NOMENCLATURE***

## ***Dimensional Variables***

- $\hat{x}$  = coordinate direction in the plane of the otoconial layer  
 $\hat{y}_f$  = coordinate direction normal to the plane of the otolith with origin at the fluid base  
 $\hat{y}_g$  = coordinate direction normal to the plane of the otolith with origin at the gel base  
 $\hat{t}$  = time  
 $\hat{u}(\hat{y}_f, \hat{t})$  = velocity of the endolymph fluid measured with respect to the skull  
 $\hat{v}(\hat{t})$  = velocity of the otoconial layer measured with respect to the skull  
 $\hat{w}(\hat{y}_g, \hat{t})$  = velocity of the gel layer measured with respect to the skull  
 $\hat{\delta}(\hat{y}_g, \hat{t})$  = displacement of the gel layer measured with respect to the skull  
 $\hat{\delta}_o(\hat{t})$  = displacement of the otoconial layer measured with respect to the skull  
 $\hat{V}_s$  = skull velocity in the x-direction measured with respect to an inertial reference frame  
 $\hat{V}$  = a characteristic velocity in the problem  
 $\hat{\tau}_g$  = gel shear stress in the x-direction  
 $\hat{\tau}_f$  = fluid shear stress in the x-direction  
 $\hat{g}_x$  = gravity component in the x-direction  
 $\hat{s}$  = the Laplace transform variable (real time)  
 $\hat{A} = - \left[ \frac{\partial \hat{V}_s}{\partial \hat{t}} - \hat{g}_x \right]$   
 $\overline{A}$  = magnitude of a step change in acceleration

## ***Dimensional Physical Constants***

(including numerical value ranges for mammalian otolithic organs)

- $\rho_o$  = density of the otoconial layer (1.35 to 2.7 x 10<sup>3</sup> kg/m<sup>3</sup>)  
 $\rho_f$  = density of the endolymph fluid (1.00 x 10<sup>3</sup> kg/m<sup>3</sup>)  
 $\mu_f$  = viscosity of the endolymph fluid (0.85 mPa s)  
 $\mu_g$  = viscosity of the gel material ( $\mu_g = M\mu_f$ ; where M=5 to 50)  
 $G$  = shear modulus of the gel material (0.1 to 10 Pa)  
 $b$  = otoconial layer thickness (5 to 20  $\mu$ m)  
 $c$  = gel layer thickness (assumed: c = b in the model derivation)



### *Nondimensional Variables*

<b>Space</b>	$y_g = \frac{\hat{y}_g}{b}$	$y_f = \frac{\hat{y}_f}{b}$		
<b>Time</b>	$t = \frac{\mu_f}{\rho_0 b^2} \hat{t}$	$s = \frac{\rho_0 b^2}{\mu_f} \hat{s}$		
<b>Velocity</b>	$u = \frac{\hat{u}}{\hat{V}}$	$v = \frac{\hat{v}}{\hat{V}}$	$w = \frac{\hat{w}}{\hat{V}}$	$V_s = \frac{\hat{V}_s}{\hat{V}}$
<b>Deflection</b>	$\delta = \frac{\mu_f}{\hat{V} \rho_0 b^2} \hat{\delta}$			

### *Nondimensional Parameters*

$R = \frac{\rho_f}{\rho_0}$	$\varepsilon = G \frac{b^2}{\mu_f^2} \rho_0$	$M = \frac{\mu_g}{\mu_f}$	$\bar{g}_x = \frac{b^2 \rho_0}{\mu_f \hat{V}} \hat{g}_x$
$A = - \left[ \frac{\partial V_s}{\partial t} - \bar{g}_x \right]$			

# Chapter 1

## *Introduction*

*“Today, world events mandate a need to project non-lethal force across all levels of war to enable our warfighters and leaders to effectively deal with a host of traditional as well as non-traditional threats. Now more than ever, the minimal level of public tolerance for collateral damage and loss of human life, coupled with the tendency for the typical adversary to exploit our rules of engagement to his benefit, necessitates an effective and flexible application of force through non-lethal weapons.”*

General James L. Jones  
32nd Commandant of the  
United States Marine Corps  
June 2000  
<http://www.jnlwd.usmc.mil/>

### **1.1 OPENING REMARKS**

The development of less-than-lethal weapon systems is a high priority program within the United States Navy research and development community (Bedard, 2000; Purificato, 2001). Predicting the effects of non-lethal weapons is essential to gain confidence in the use of non-lethal force. When faced with the decision to use non-lethal weapons, commanders must be able to confidently predict the most probable effects on targets. To achieve this level of confidence, the health effects of non-lethal weapons on humans must be completely understood, and these effects must be accurately assessed in real-time. Modeling, simulation, and experimentation will provide a means of gathering acceptable data that can be extrapolated and used for the analysis of the effects of non-lethal weapons on humans.

Non-lethal weapons research is relevant to the topics of otolith organ modeling and monitoring because stimulating the otolith organs and other parts of the vestibular system outside of their normal ranges of perception/function has been shown to cause symptoms of disequilibrium, transient visual frame shifts, spontaneous nystagmus (rapid eye movements) and motion sickness. These effects could conceivably be used to incapacitate a foe. Some U.S. Navy Divers, exposed to high intensities of low frequency sound, have suffered reversible, but long-lasting symptoms consistent with intense vestibular stimulation (Steevens, Russell, Knafelc, Smith, Hopkins, and Clark, 1999). Hence, the vestibular system is a likely target for a non-lethal weapon. The modeling and experimentation presented in this work is useful for developing both non-lethal weapons and protection for Navy personnel against such weapons.

## **1.2 VESTIBULAR SYSTEM**

The vestibular system, located within the inner ear, plays a crucial role in balance and posture, stabilization of eye movements, and spatial orientation. The vestibular system consists of two distinct types of sensors; one, the semicircular canals which detect angular acceleration and two, the otolith organs which detect linear acceleration.

A simplified summary of vestibular function is put forth by Kelly (1991). “The vestibular labyrinth has two interrelated functions. The *dynamic* function, mediated principally by the semicircular ducts enables us to track the rotation of the head in space and is important for the reflex control of eye movements. Since there are no steady-state

angular forces that affect the head, the semicircular ducts serve a uniquely dynamic function. The *static* function, mediated principally by the utricle and saccule [in response to gravity], enables us to monitor the absolute position of the head in space, and this plays a pivotal role in the control of posture. The utricle and saccule also detect linear accelerations, so in actuality they have both a static and dynamic function.”

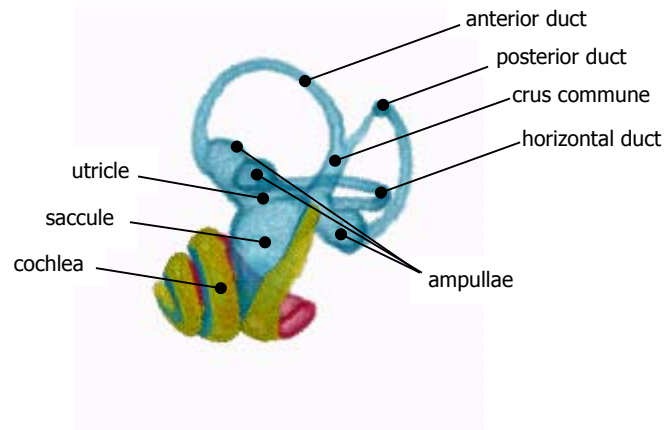


**Figure 1.1 – The membranous labyrinth of the inner ear. From a 3-D reconstruction of a gerbil MRI scan (reproduced with permission from Henson 2000).**

The vestibular system is comprised of a membranous labyrinth that is supported by fibrous connections inside a contoured bony labyrinth in the temporal bone of the skull, adjacent to, and in communication with, the cochlea of the inner ear. The membranous labyrinth, shown in Figure 1.1, forms a closed system filled with a fluid called endolymph. Looking at the membranous labyrinth one sees three semicircular ducts, or canals. The anterior, the posterior and the horizontal, semicircular ducts project from a single cavity, the utricle, to form three almost orthogonal closed loops. The horizontal duct is separate from the anterior and posterior ducts and the latter two merge over a

portion of their length to form a common crus that enters the top of the utricle. At one end of each duct is an enlarged section known as the ampulla, which contains the sensory portion of the angular motion detector. The ampullae of the three semicircular canals are attached to the utricle. The utricle and saccule, again nearly mutually orthogonal, contain the sensory portion of the linear acceleration detectors, or otolith organs.

As shown in Figure 1.2, the ampulla contains the crista, a saddle-shaped ridge that extends across the bottom of the ampulla at right angles to the long axis. The crista contains specialized hair cells, whose sensory cilia extend upward into the cupula.

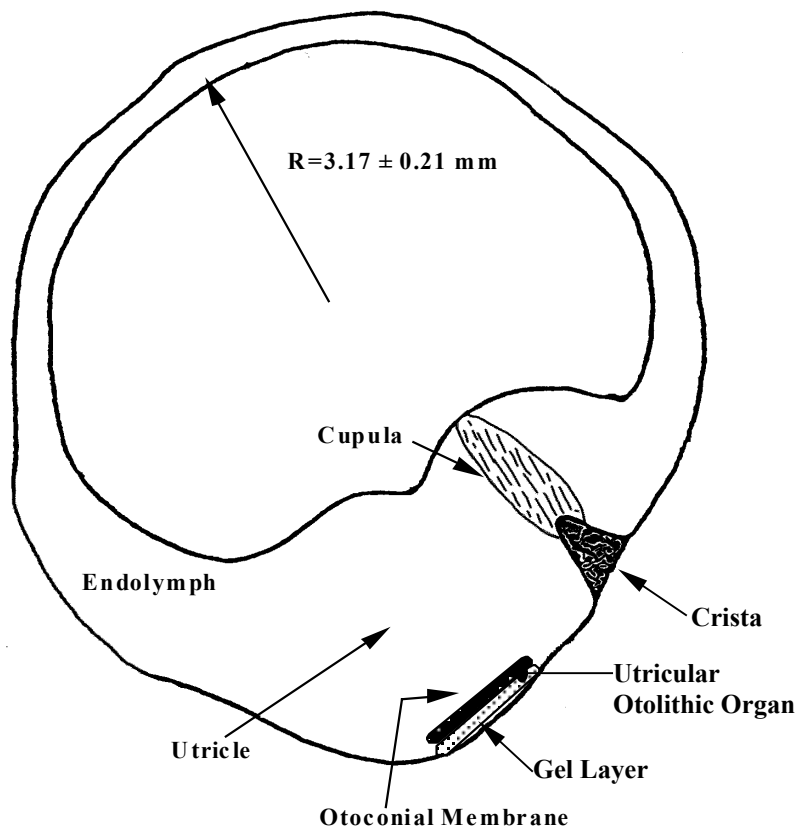
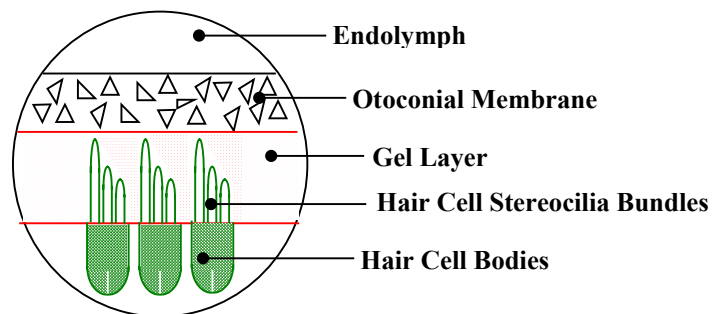


Figure 1.2 – Schematic of the horizontal semicircular canal and utricle.

The cupula is a fragile, transparent, elastic membrane, composed of a saccharide gel that extends from the crista to the roof of the ampulla with its edge contacting the membranous wall all the way around the ampulla forming a fluid tight partition. The cupula thus interrupts the otherwise continuous endolymph-fluid path through the duct, utricle, and ampulla. Movement of the head causes fluid motion of the endolymph to deform the cupula, which results in deflecting the sensory hair cell cilia and initiating a neural signal reporting angular acceleration to the central nervous system. Also shown in Figure 1.2 is the utricular otolithic organ, or macula utriculus. A nearly identical structure is present in the saccule and is known as the macula sacculus. These are the organs that sense linear accelerations and static head tilt. Each organ is composed of an otoconial membrane attached to an elastic gel layer that contains stereocilia bundles of sensory hair cells, and is fixed to the utricle wall. A cross-sectional diagram of the organ structure is presented in Figure 1.3. The otoconial membrane is fixed only to the gel layer and is free to move in two dimensions within the elastic limits of the gel layer. Movement of the otoconial membrane causes shearing in the gel layer, which in turn deflects the stereocilia bundles causing a neural signal to report linear acceleration to the central nervous system.



**Figure 1.3 – Cross-section of an otolithic organ.**

The central nervous system uses the vestibular information in different ways. One is to generate eye movements that stabilize vision when head and body motion would otherwise result in a blurred image. The vestibular signals also supplement vision for body orientation and equilibrium data, and provide information for both skilled and reflexive motor activities. The vestibular system provides, in the absence of visual cues, a reasonably accurate perception of motion and position of the head within a certain range of stimulation. Although the basic role of the vestibular system is known, many details of its function are not well understood.

The mammalian vestibular system is well adapted to function accurately within the realm of normal motor activities; however, technology has created certain situations that stimulate the vestibular system beyond its normal physiological range. The inability of the vestibular system to function in these abnormal conditions can result in illusions, spatial disorientation and motion sickness. The occurrence of vestibular illusions during aerospace flight is well documented (Benson, 1999; Gillingham and Previc, 1996). A lesser-known cause of abnormal vestibular response is sound. Certain frequencies can stimulate the natural resonant frequencies of the otolith organs resulting in false neural outputs. In underwater situations the deleterious effects of sound on the organs is intensified as sound is transmitted more freely in this medium.

Improved understanding of the mechanics of the vestibular system will not only improve our understanding of vestibular-based non-lethal weapons, but will also lead to improvements in neuro-otological diagnoses and treatment. For development of more

and better clinical otolith function tests, precise descriptions of how the organs work are needed. Improved understanding of physical events in neuro-otological disorders will lead to improvements in the diagnosis and treatment of these disorders. Another benefit of detailed knowledge of the vestibular system will be overcoming vestibular system limitations in environments outside of its normal range of stimulation, such as aerospace flight.

### **1.3 THESIS GOALS**

The goal of this thesis is to provide some basic research in support of the United States Navy's effort to investigate and implement vestibular based non-lethal weapons. This is approached in three different ways. The first is to develop a simple mathematical model relating otoconial displacement to input stimulus. The key feature of this model is its simplicity. Requiring minimal processing to solve, it can easily be solved real-time. The second area of research addressed in this thesis is finite element modeling of the otolith organs. A simple two-dimensional model is presented that shows organ deformation under different applied loads. This represents the first attempt to develop a finite element model that includes hair cell bundles along with the gel and otoconial layers. While modeling predicts the vestibular response, it is still necessary to measure vestibular output both to obtain data to improve and verify models and also to study the response of the vestibular system to stimulus. The third and final area of research presented here is a technique to monitor the output of the vestibular system in a United States Navy operating environment. Due to the location of the vestibular system in the skull, as



described above, the vestibular nerve is basically inaccessible in humans for experimental purposes. Some direct vestibular neural recordings have been obtained in animals (Goldberg, Desmadryl, Baird, and Fernandez, 1990), but for humans, other methods must be used. Because the vestibular system is responsible for controlling reflex eye movements, eye movements can be used to gauge vestibular function. A likely application for a vestibular-based non-lethal weapon is in an underwater environment where sound is freely transmitted. A means for monitoring eye movements in this setting is presented.

## **1.4 THESIS ORGANIZATION**

Chapter 1 provides an introduction to non-lethal weapons and the vestibular system and outlines the work presented in this thesis.

Chapter 2 describes the development of a simplified transfer function relating otoconial membrane displacement to input stimulus. The model is tested against results from a more complex transfer function.

Chapter 3 presents a two-dimensional finite element model of a mammalian utricular macula. Deformation of the organ under an acceleration stimulus is shown, along with natural frequencies and mode shapes.

Chapter 4 presents an experiment in which a technique to measure vestibular response to underwater sound is developed. Eye movements of divers exposed to low frequency high intensity sound are recorded and analyzed for vestibular nystagmus.

Chapter 5 summarizes the findings of the research presented herein.

## *Chapter 2*

# *A Simplified Mathematical Model to Predict Otolith Membrane Displacement*

### **2.1 PREVIOUS MATHEMATICAL MODELS**

The objective of this work is to develop a simplified mathematical model of the otolithic organs that describes dynamic and time response to an input stimulus. The term ‘otolithic organs’ refers to both the utricle and the saccule. The model used here to describe the mechanical response of these organs is generic. It represents the mechanical response of both the utricle and saccule. The author recognizes the differences between the utricle and saccule; however, the present analysis emphasizes their mechanical similarities. The organ is modeled as a three-layer system comprised of a gel layer, an otoconial membrane, and an endolymph fluid layer. For simplicity, each layer is treated as a continuum with uniform properties throughout. This means that both striolar region effects, as well as the complexities of the gel layer as pointed out by Kachar, Parakkal, and Fex (1990) are neglected.

Previously, distributed parameter models were developed that characterized function and provided a fundamental understanding of the mechanical transduction process (Grant and Cotton, 1990/91; Grant, Best, and LoNigro, 1984; Hudetz, 1973; Kondrachuk, Schehechkin, and Sirenko, 1986). These models were solved numerically in the time domain; and, these solutions were used to determine the range of parameters that are appropriate for correct otolithic mechanical function. Additional work established the frequency response for the mechanical model (Grant, Huang, and Cotton, 1994). The complexity of these earlier models does not allow for direct analytic time domain solutions. The current effort is aimed at simplifying this earlier work into a usable lumped parameter model where time is the only independent variable.

A set of partial differential equations was derived in earlier work by applying the equations of motion to free-body analysis of the forces acting on the otoliths (Grant *et al.*, 1984; Grant *et al.*, 1990/91). The free-body diagrams are shown in Figure 2.1. The equation set, as written below, is in dimensionless form and assumes motion in one dimension only. Consult the nomenclature table and the earlier work for definitions of the variables involved. There are several dimensionless parameters that arise naturally in the nondimensionalization process; they are  $R$ ,  $\epsilon$ , and  $M$ . The density ratio between endolymph fluid and otoconia,  $R$ , can be thought of as controlling the magnitude of the displacement (it does not represent the system mass but can be visualized as such),  $\epsilon$  represents the elastic or restorative modulus of the system, and  $M$ , the ratio of gel viscosity to fluid viscosity, represents the major portion of system damping. Again see the nomenclature table for definitions of these nondimensional parameters.

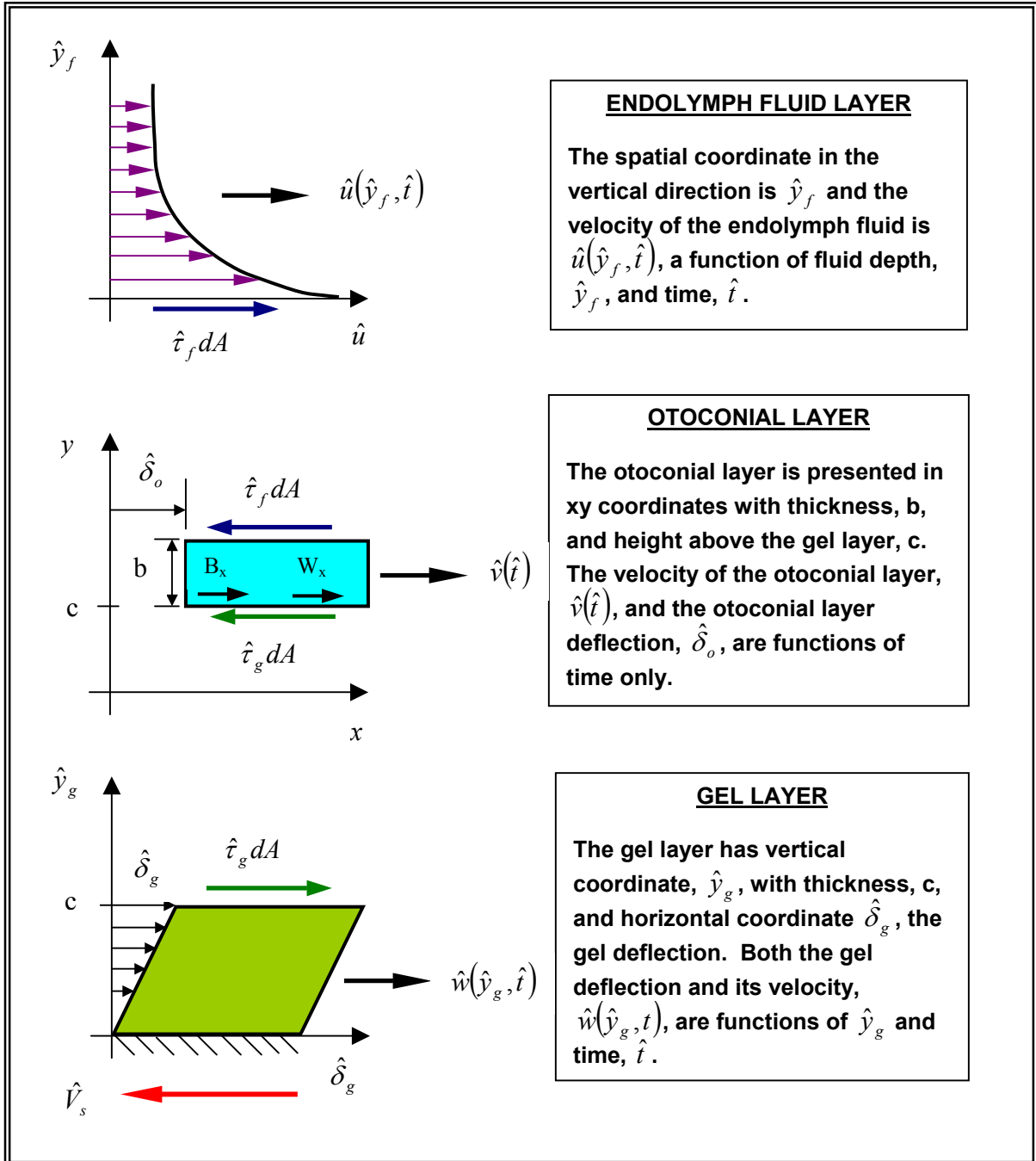


Figure 2.1 – Free-body force diagrams of the otoconial layer, endolymph fluid layer, and gel layer. The interfaces are coupled by shear stresses of equal magnitude that act in opposite directions on each surface. The forces acting at these interfaces are the product of shear stress,  $\tau$ , and area,  $dA$ . The  $B_x$  and  $W_x$  forces are the components of the buoyant and weight forces acting in the plane of the otoconial layer.  $\hat{V}_s$  is the skull velocity.

The coupled partial differential equation set describing the dynamics of the otolith system is:

$$\text{Endolymph Fluid Layer} \quad R \frac{\partial u}{\partial t} = \frac{\partial^2 u}{\partial y_f^2} \quad (2.1)$$

$$\begin{aligned} \text{Boundary Conditions} \quad u(0, t) &= v(t) \\ u(\infty, t) &= 0 \end{aligned} \quad (2.2)$$

$$\text{Initial Condition} \quad u(y_f, 0) = 0 \quad (2.3)$$

**Otoconial Layer**

$$\frac{\partial v}{\partial t} + (1 - R) \left[ \frac{\partial V_s}{\partial t} - \bar{g}_x \right] = \frac{\partial u}{\partial y_f} \Big|_{y_f=0} - \varepsilon \int_0^t \frac{\partial w}{\partial y_g} \Big|_{y_g=1} dt - M \frac{\partial w}{\partial y_g} \Big|_{y_g=1} \quad (2.4)$$

$$\begin{aligned} \text{Initial Conditions} \quad v(0) &= 0 \\ \delta_0(0) &= 0 \end{aligned} \quad (2.5)$$

**Gel Layer**

$$R \frac{\partial w}{\partial t} = \varepsilon \int_0^t \frac{\partial^2 w}{\partial y_g^2} dt + M \frac{\partial^2 w}{\partial y_g^2} \quad (2.6)$$

$$\begin{aligned} \text{Boundary Conditions} \quad w(1, t) &= v(t) \\ w(0, t) &= 0 \end{aligned} \quad (2.7)$$

$$\begin{aligned} \text{Initial Conditions} \quad w(y_g, 0) &= 0 \\ \delta_g(y_g, 0) &= 0 \end{aligned} \quad (2.8)$$

The detailed derivations of these equations can be found in the previous published work (Grant *et al.*, 1984; Grant *et al.*, 1990/91). These equations are solved in the time domain by using finite difference numerical techniques; and, these solutions will be used as the

standard against which the time domain results obtained from the simplified model developed in this work are compared. The dimensionless nature of these equations shall be retained for the simplification process and for initial comparisons. Conversion to dimensional form will be delayed until time constants are evaluated and the final time domain results are developed.

A transfer function, which relates otoconial layer displacement to acceleration, was also developed in the earlier work from Equations 1 through 8 (Grant *et al.*, 1994). To develop this transfer function, the Laplace transform of each partial differential equation is taken with respect to time. The transformed equations are then combined into a single function that contains the spatial variables  $y_g$  and  $y_f$ . These variables are eliminated from the resulting transfer function by evaluating it at the spatial location of the otoconial layer. This function is shown below and relates otoconial layer displacement  $\delta_0$  to acceleration  $A$ , where acceleration is defined as the sum of skull acceleration  $a_x$  and gravity  $g_x$  [ $A=(a_x-g_x)$ ]; and, where  $s$  is the Laplace transform variable:

$$\frac{\delta_0}{A}(s) = \frac{(1-R)}{s \left[ s + \sqrt{Rs} + \left( \frac{\varepsilon}{s} + M \right) \sqrt{\frac{Rs}{\frac{\varepsilon}{s} + M}} \coth \left( \sqrt{\frac{Rs}{\frac{\varepsilon}{s} + M}} \right) \right]} \quad (2.9)$$

A frequency response analysis of the above transfer function is performed by substituting  $j\omega$  for the Laplace transform variable  $s$ . With this substitution, Bode plots of magnitude and phase angle versus frequency are generated. Due to the complexity of the transfer function, it is necessary to employ numerical techniques to perform the frequency

response analysis. The resulting Bode plots from the full transfer function will be used as the standard for comparison for Bode plots obtained from the simplified model. In addition, frequency response results from the simplified transfer function will be compared to experimental first-order neuron frequency data. This will provide a biologic validation of the resulting simplified model.

To obtain an analytic time domain solution of the transfer function, it is necessary to perform an inverse Laplace transform on Equation 2.9. If a full solution, with spatial variations included, is desired, the transfer function with spatial variations must be inverted. However, attempts at inverting the transfer function of Equation 2.9, or the one that includes spatial variables, have proven to be difficult, complex, and unworkable. The difficulty of inversion is primarily due to the  $\sqrt{s}$  term and the transcendental function *coth*. These terms in the transfer function make the inversion extremely difficult if not impossible. In addition, if an inverse time domain solution were obtained, the resulting time domain function would likely also be complex and unmanageable from a practical standpoint. As a result, a simplified approximation of the full inversion solution would probably have to be developed for working purposes. It then seems appropriate to develop a simplified transfer function that can easily be inverted to a workable time domain solution.



## 2.2 SIMPLIFYING A COMPLEX TRANSFER FUNCTION

The goal of this section is to seek a simplified transfer function that will yield analytic time domain solutions that are comparable to those obtained numerically from the complete transfer function, Equation 2.9. This simplification is accomplished by introducing approximations for both the  $\sqrt{s}$  and  $\coth$  terms. The resulting modified transfer function will make analytic time domain solutions possible for various acceleration input stimuli; and more importantly, will facilitate the evaluation of system time constants.

Approximations for the  $\sqrt{s}$  and  $\coth$  are found by expanding each of these terms in a Taylor series. The  $\coth$  is tackled first. The definition for  $\coth$  is:

$$\coth(x) = \frac{e^x + e^{-x}}{e^x - e^{-x}} \quad (2.10)$$

To obtain a Taylor series expansion for  $\coth$ ,  $e^x$  is expressed in a Taylor series about the point zero and then substituted into the definition of  $\coth$ . The algebraic manipulation of this expression results in the following series approximation:

$$\coth(x) = \frac{1}{x} + \frac{x}{3} - \frac{x^3}{45} + \frac{2x^5}{945} + \dots \quad (2.11)$$

where  $x$  is the argument of the function. This approximation proves to be adequate over the entire range of the argument  $x$  utilized for the current application where:

$$x = \sqrt{\frac{Rs}{\frac{\varepsilon}{s} + M}} \quad (2.12)$$

As an initial effort to simplify the transfer function, the first three terms of the *coth* series are arbitrarily chosen to replace the original function. Making this substitution and collecting like terms yields the following:

$$\frac{\delta_0}{A}(s) = \frac{(1-R)}{\left( -\frac{1}{45} \frac{R^2}{\left( \frac{\varepsilon}{s} + M \right)} \right) s^3 + \left( 1 + \frac{R}{3} \right) s^2 + (M + \sqrt{Rs})s + \varepsilon} \quad (2.13)$$

Note that the appearance of the  $s^3$  term has changed the fundamental nature of what should be a second-order system.

Frequency response analyses are performed for the approximate transfer function with a three-term *coth* approximation, a two-term *coth* approximation, and a single-term *coth* approximation. The results are compared with results from the complete TF and are plotted in Figure 2.2. Values for the nondimensional variables are set at  $R=0.5$ ,  $\varepsilon=0.2$ , and  $M=10$  for this comparison.

Repeating this comparison over the full range of values of the nondimensional parameters yields similar results. In Figure 2.2, it can be seen that results from both the two-term approximation and the one-term approximation closely match the full transfer function results. It is not surprising that the three-term approximation is not a good match because the system is basically second order. The two-term representation is

perhaps slightly better than the one-term representation, however, the single-term will be chosen for simplicity (the single-term approximation also proves to yield better time response results).

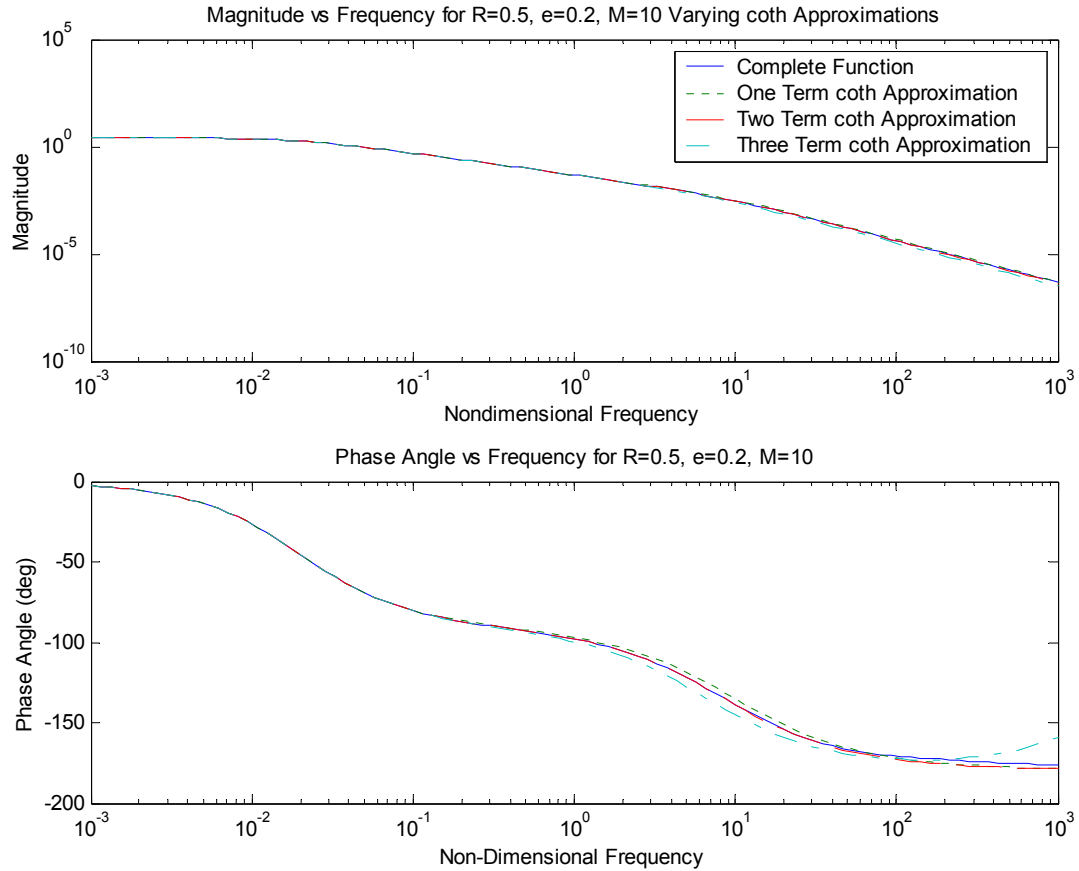


**Figure 2.2 – Frequency response diagram of the complete transfer function compared with approximations where the coth term is replaced with one, two, or three terms of a Taylor series expansion. In this comparison the  $\sqrt{s}$  term is retained in full so that only the effects of the coth approximations are evaluated. Values for the nondimensional variables for the comparisons are  $R=0.5$ ,  $e=0.2$ , and  $M=10$ . The single-term approximation is chosen for use in the simplified transfer function. The two-term approximation is almost an exact match, however, the one-term approximation is good and less complex. By choosing the less complex single-term approximation, the resulting transfer function is simplified; and, the time response results are as good as with the more complex two-term approximation.**

The resulting transfer function with a single -term approximation for the *coth* is:

$$\frac{\delta_0}{A}(s) = \frac{(1-R)}{s^2 + (M + \sqrt{Rs})s + \varepsilon} \quad (2.14)$$

To find a suitable approximation for the  $\sqrt{s}$  term, the sequence described above is repeated. First,  $\sqrt{s}$  is expanded in a Taylor series about the point 1. The point 1 is chosen as it yields a good series approximation for  $\sqrt{s}$  over the range of  $s$  relevant to the frequency and time response analysis of the transfer function. Other expansion points were tested, but 1 proved to be the best choice. Next, frequency response analyses are performed for the transfer function with a three-term  $\sqrt{s}$  approximation, a two-term  $\sqrt{s}$  approximation, and a single-term  $\sqrt{s}$  approximation. The different approximations are as follows:

$$\text{One-term expansion} \quad \sqrt{s} = 1 \quad (2.15)$$

$$\text{Two-term expansion} \quad \sqrt{s} = \frac{1}{2} + \frac{1}{2}s \quad (2.16)$$

$$\text{Three-term expansion} \quad \sqrt{s} = \frac{3}{8} + \frac{3}{4}s - \frac{1}{8}s^2 \quad (2.17)$$

Frequency response results utilizing the above approximations are compared with results from the complete transfer function in Figure 2.3. It should be noted that the *coth* term is retained in this comparison. Values for the nondimensional variables are once again set at  $R=0.5$ ,  $\varepsilon=0.2$ , and  $M=10$ .

Results from both the single-term  $\sqrt{s}$  approximation and the two-term  $\sqrt{s}$

approximation correlate well with results from the full transfer function. It is also worth mentioning that the complete elimination of the  $\sqrt{s}$  term from the transfer function provides frequency response analysis results that are a good match to results from the complete transfer function.

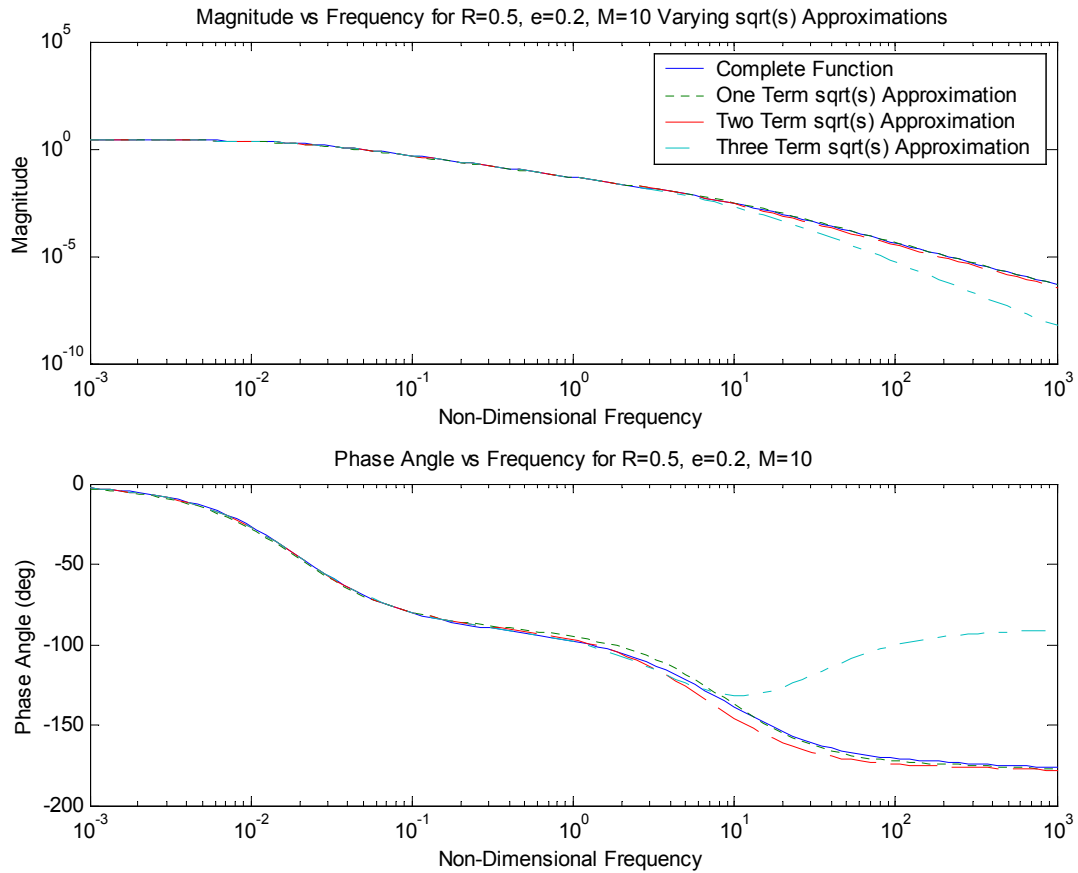


**Figure 2.3 – Frequency response diagram of the complete transfer function compared with approximations where the  $\sqrt{s}$  term is replaced with one, two, or three terms of a Taylor series expansion. In this comparison the  $\coth$  term is retained in full so that only the effects of the  $\sqrt{s}$  approximations are evaluated. Values for the nondimensional variables for the comparisons are  $R=0.5$ ,  $\varepsilon=0.2$ , and  $M=10$ . The two-term approximation is chosen for use in the simplified transfer function. The two-term approximation is a good match over the entire frequency range and proves to be a much better match in the time domain solutions than either the one-term or three-term approximations.**

The complete elimination of the  $\sqrt{s}$  term physically represents the elimination of the endolymph fluid damping produced by contact of the top of the otoconial layer with endolymph. Even though completely eliminating  $\sqrt{s}$  from the transfer function would be the most straightforward simplification, it turns out that it is necessary to retain this term in order to produce valid time response solutions from the simplified transfer function. The  $\sqrt{s}$  approximation that provides the best results for both frequency and time response analyses is the two-term expansion.

## 2.3 THE SIMPLIFIED MODEL

The final simplified version of the transfer function, which includes a single term Taylor series approximation for  $\coth$  and a two term Taylor series approximation for  $\sqrt{s}$ , is:

$$\frac{\delta_0}{A}(s) = \frac{(1-R)}{\left(1 + \frac{\sqrt{R}}{2}\right)s^2 + \left(M + \frac{\sqrt{R}}{2}\right)s + \varepsilon} \quad (2.18)$$

Because the exact values of the nondimensional parameters M,  $\varepsilon$ , and R are not known, it is necessary to test the simplified transfer function over their expected range of values. These results are shown in Figures 2.4, 2.5, and 2.6.

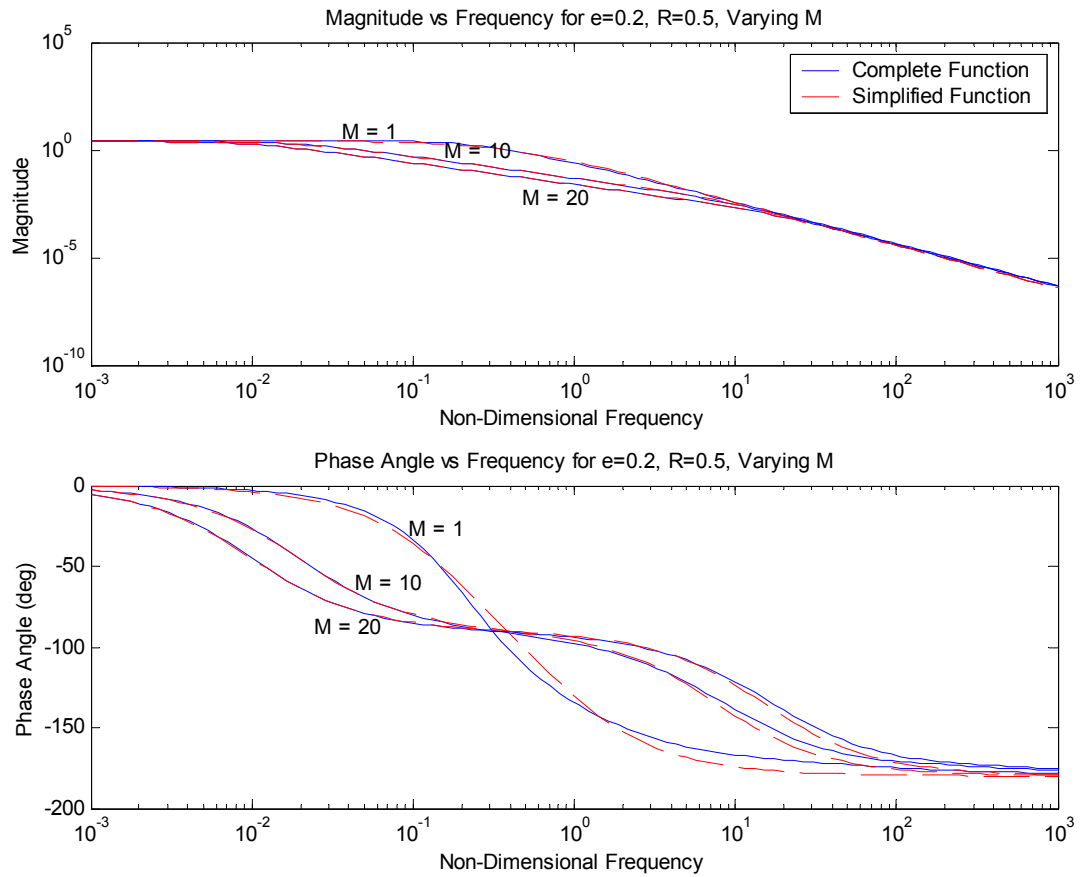


**Figure 2.4 – Frequency response diagram of the complete transfer function compared with the final version of the approximate transfer function showing the effects of the nondimensional variable M. Here M is varied over its likely range, 1 – 20, while  $\epsilon$  and R are held constant at 0.2 and 0.5, respectively.**

Over the full range of the nondimensional variables, the simplified transfer function yields results that are quite good when compared to results from the full complete transfer function. These matches indicate that the simplified transfer function is an excellent approximation to the full transfer function.

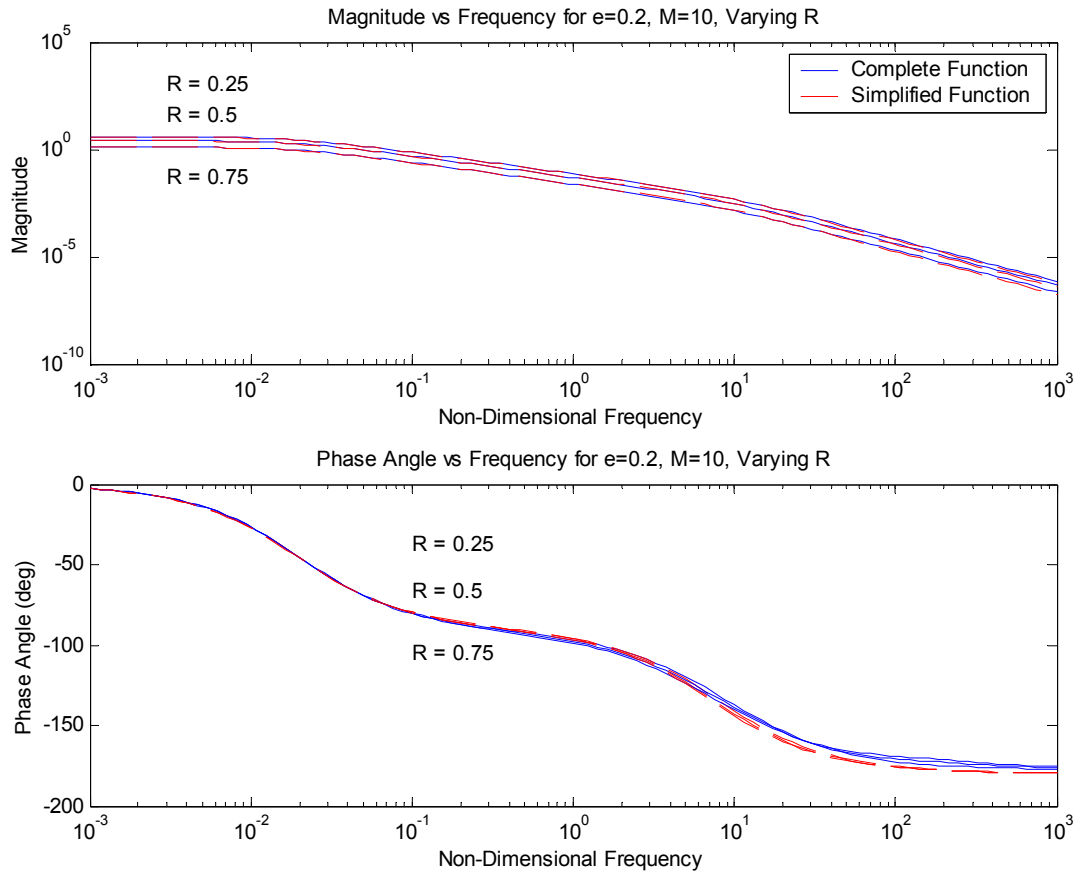


**Figure 2.5 – Frequency response diagram of the complete transfer function compared with the final version of the approximate transfer function showing the effects of the nondimensional variable  $R$ . Here  $R$  is varied over its likely range, 0.25 – 0.75, while  $\varepsilon$  and  $M$  are held constant at 0.2 and 10, respectively.**

For biologic validation of the model, its frequency response results are compared to experimental frequency response data. Recordings of chinchilla first order neuron responses are presented by Goldberg, *et al.* (1990) and are used for the comparison. To carry out this comparison, it is necessary to convert the model's frequency response output from nondimensional units into Hertz. This conversion is accomplished by taking the reciprocal of real time using the real-to-nondimensional time conversions shown in the nomenclature table. This produces a radians-per-second frequency, which is easily



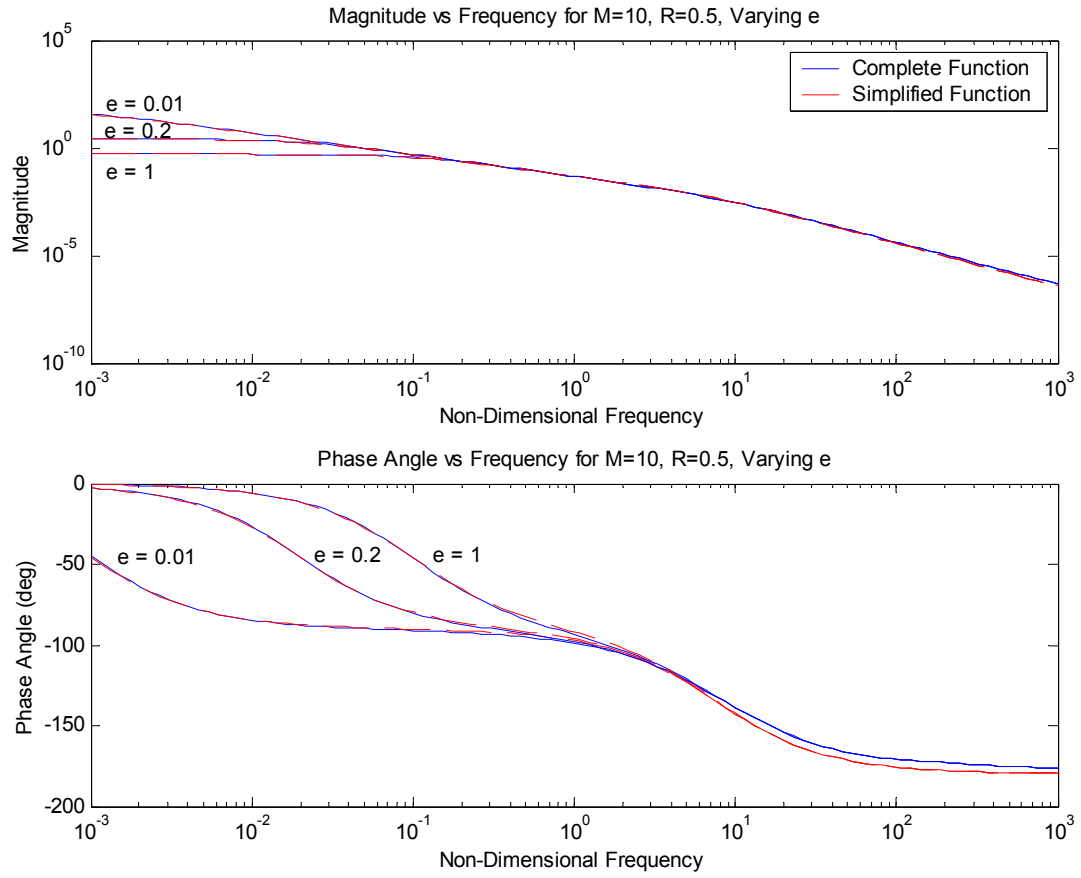


**Figure 2.6 – Frequency response diagram of the complete transfer function compared with the final version of the approximate transfer function showing the effects of the nondimensional variable  $\epsilon$ . Here  $\epsilon$  is varied over its likely range, 0.01 – 1, while R and M are held constant at 0.5 and 10, respectively.**

converted into Hertz. Results are presented in Figure 2.7. The frequency response, predicted by the model, closely follows the actual recorded frequency response over most of the range. Discrepancies at the low-frequency end of the spectrum are thought to be non-mechanical, originating rather from a cellular or neural transmission source. A significant result is that we have matched the corner frequency of the experimental data with a mathematical simplification of the governing equations. Matching the

experimental frequency response data with results from the simplified transfer function, lends biologic credibility to the model.

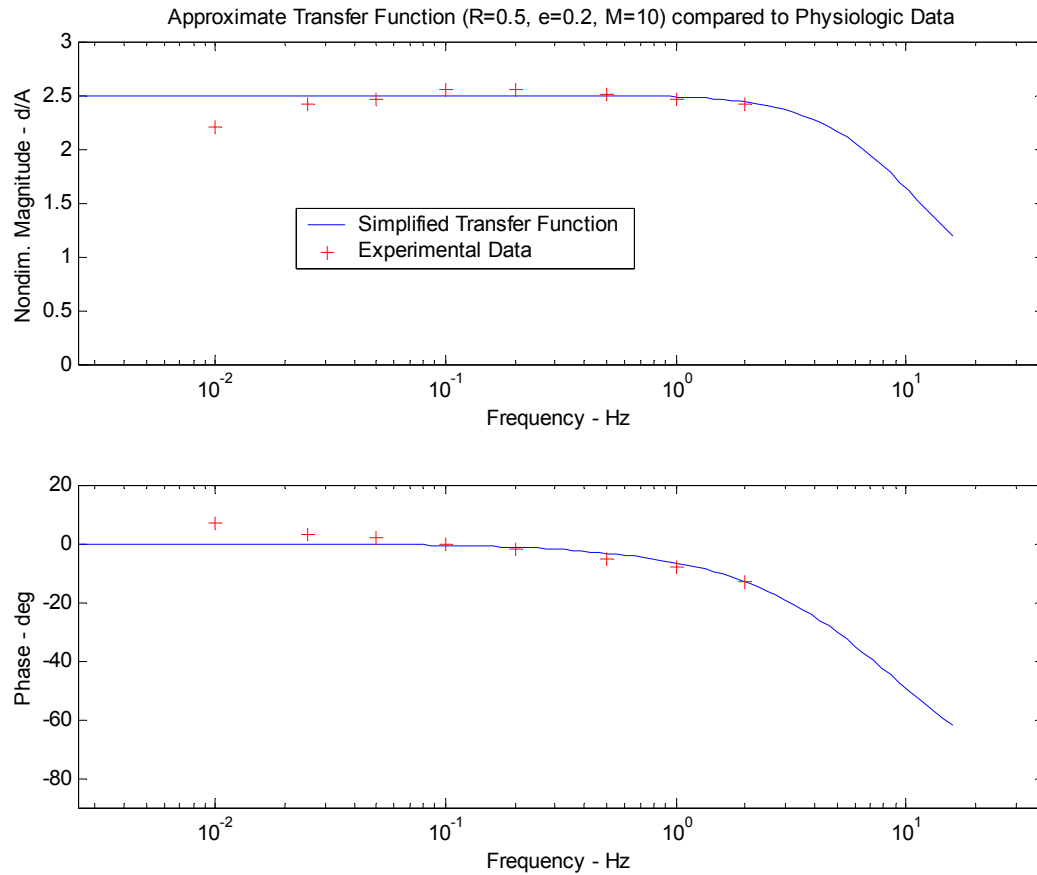


**Figure 2.7 – Frequency response of the simplified transfer function, Equation 2.18, compared to experimental data from Goldberg *et al.* (1990). The simplified transfer function curve was fit to the utricular neural afferent data by using a regression analysis where  $\varepsilon$  and  $M$  were allowed to vary, and  $R$  was held constant. The magnitude of the experimental data had been normalized, and the simplified transfer function curve was shifted upward to match the experimental data. This shifting was accomplished by matching the flat response portion of the curve to the average of the middle four data points, which produced a simple shifting upward. The phase curve was unchanged. The low-frequency amplitude attenuation and phase lead of the physiologic data are probably due to nonmechanical effects.**

The theoretical transfer function, from which the simplified model is developed, is derived from first principles. The ranges of values utilized in the model for the nondimensional parameters  $M$ ,  $R$ , and  $\varepsilon$  are selected based on certain criteria. These

criteria are that the system must have an over damped response; and, that the otoconial layer deflection must be within realistic physiologic bounds. All of these things combined, produce a transfer function that has theoretical roots and can be validated by comparison with experimental data.

## 2.4 A PHYSICAL SIMPLIFICATION

The foregoing analysis is a purely mathematical simplification of a complex equation set resulting in a transfer function that describes otoconial layer displacement. No physical significance was attached to the simplification process. It is interesting to note that, by making some physical assumptions about the otolith organ and applying them to the original governing equations, one can simplify the complex equation set to achieve a similar result as the mathematical simplification. Equation 2.4 is the governing equation of motion of the otoconial layer. If we make two physical assumptions, numbered below:

1). that the velocity profile in the gel layer is linear:

$$\frac{\partial w}{\partial y} = v(t) \quad (2.19)$$

and

2). that the fluid shear is negligible:

$$\frac{\partial u}{\partial y} = 0 \quad (2.20)$$

we can simply 2.4 to:

$$\frac{\partial v}{\partial t} + (1 - R) \left[ \frac{\partial V_s}{\partial t} - \bar{g}_x \right] = -\varepsilon \int_0^t v dt - Mv \quad (2.21)$$

If we now apply a Laplace transform the result is:

$$\frac{v(s)}{A} = (1 - R) \frac{1}{s + \frac{\varepsilon}{s} + M} \quad (2.22)$$

Remembering the relationship:

$$\delta_o(s) = \frac{v(s)}{s} \quad (2.23)$$

We can simplify the transfer function to:

$$\frac{\delta_o}{A} = \frac{(1 - R)}{s^2 + Ms + \varepsilon} \quad (2.24)$$

This is the same as the mathematical simplification (Equation 2.18) if you eliminate the square root of R term in Equation 2.18. To investigate the origin of the square root of R term we must return to the derivation of our original transfer function (presented fully in earlier work (Grant *et al.*, 1994)). We find that as we take the Laplace transform of the original governing equations we get expressions for the velocity profile in the gel layer and the fluid shear. From the Laplace transform of the gel equation (2.6) we get:

$$\frac{\partial w}{\partial y} = v(s) \frac{\sqrt{\frac{Rs}{\varepsilon + Ms}} \coth \sqrt{\frac{Rs}{\varepsilon + Ms}}}{\sqrt{\frac{\varepsilon}{s} + M}} \quad (2.25)$$

Our mathematical *coth* approximation is:

$$\coth \left( \sqrt{\frac{Rs}{\varepsilon + Ms}} \right) \approx \sqrt{\frac{\varepsilon + Ms}{Rs}} \quad (2.26)$$

Substituting back we find the expression used for the gel layer velocity profile in the mathematical simplification. It is:

$$\frac{\partial w}{\partial y} = v(s) \quad (2.27)$$

This says the gel layer velocity profile is linear, which is the same as physical assumption 1.

From the Laplace transform of the fluid equation (2.1) we get:

$$\frac{\partial u}{\partial y} = -v(s)\sqrt{R}\sqrt{s} \quad (2.28)$$

Our mathematical approximation for the square root of s is:

$$\sqrt{s} \approx \frac{1}{2} + \frac{1}{2}s \quad (2.29)$$

Substituting, we get the expression used for fluid shear in our mathematical simplification:

$$\frac{\partial u}{\partial y} = -v(s)\sqrt{R}\left(\frac{1}{2} + \frac{1}{2}s\right) \quad (2.30)$$

Comparing this result with physical assumption 2 shows that the mathematical simplification includes an expression for fluid shear while the physical simplification does not. If we had chosen zero as a mathematical simplification for the square root of s, then our mathematical simplification would be the same as the physical simplification

Looking at the physical simplification and then going back to our mathematical derivation allows us to attach some physical significance to the mathematical simplification. We can see that the square root of R term in the mathematically simplified transfer function comes from fluid damping. It originates as the coefficient of square root s in the expression for fluid shear. In the mathematical simplification we

have retained fluid damping while simplifying it; and we have effectively assumed a linear deformation profile in the gel layer. Had we approached this simplification from a physical rather than mathematical viewpoint, we likely would not have succeeded in developing an accurate simplification for the governing transfer function.

## 2.5 DIMENSIONAL FORM OF THE APPROXIMATE TRANSFER FUNCTION

Since the system response is over damped and the transfer function is second order, it is possible to factor the denominator of the transfer function into two first-order terms. The factored transfer function will be of the form:

$$\frac{\delta_0}{A}(s) = \frac{1}{\left(s + \frac{1}{T_L}\right)\left(s + \frac{1}{T_S}\right)} \quad (2.31)$$

where  $T_L$  and  $T_S$  are the system long and short time constants, respectively. Factored in this manner, the nondimensional transfer function becomes:

$$\frac{\delta_0}{A}(s) = \frac{(1-R)}{\left(1 + \frac{1}{2}\sqrt{R}\right)} \frac{1}{\left(s + \frac{\varepsilon}{\left(M + \frac{1}{2}\sqrt{R}\right)}\right)\left(s + \frac{\left(M + \frac{1}{2}\sqrt{R}\right)}{\left(1 + \frac{1}{2}\sqrt{R}\right)}\right)} \quad (2.32)$$

where the assumption  $\frac{\varepsilon}{\left(M + \frac{1}{2}\sqrt{R}\right)} \ll \frac{\left(M + \frac{1}{2}\sqrt{R}\right)}{\left(1 + \frac{1}{2}\sqrt{R}\right)}$  was utilized.

This expression can be converted to a dimensional version by substituting the dimensional equivalents for all nondimensional variables. Making these substitutions yields the following dimensional transfer function:

$$\frac{\hat{\delta}_0}{\hat{A}} = \frac{\left(1 + \frac{\rho_f}{\rho_0}\right)}{\left(1 + \frac{1}{2}\sqrt{\frac{\rho_f}{\rho_0}}\right)} \frac{1}{\left(\hat{s} + \frac{\frac{G}{\mu_f}}{\left(\frac{\mu_g}{\mu_f} + \frac{1}{2}\sqrt{\frac{\rho_f}{\rho_0}}\right)}\right) \left(\hat{s} + \frac{\left(\frac{\mu_g}{\mu_f} + \frac{1}{2}\sqrt{\frac{\rho_f}{\rho_0}}\right) \frac{\mu_f}{\rho_0 b^2}}{\left(1 + \frac{1}{2}\sqrt{\frac{\rho_f}{\rho_0}}\right)}\right)} \quad (2.33)$$

Consult the nomenclature table for the meaning of all dimensional variables  $(\hat{\delta}_0, \hat{A}, \hat{s})$  and physical constants.

Dimensional system time constants can now readily be identified from the transfer function of Equation 33, they are:

$$T_L = \frac{\left(\frac{\mu_g}{\mu_f} + \frac{1}{2}\sqrt{\frac{\rho_f}{\rho_0}}\right)}{\frac{G}{\mu_f}} \quad (2.34)$$

$$T_S = \frac{\left(1 + \frac{1}{2}\sqrt{\frac{\rho_f}{\rho_0}}\right) \rho_0 b^2}{\left(\frac{\mu_g}{\mu_f} + \frac{1}{2}\sqrt{\frac{\rho_f}{\rho_0}}\right) \mu_f} \quad (2.35)$$

With these expressions for the two time constants, it is now possible to calculate their numerical values. Since exact values are not known for the various physical parameters in the equations, ranges of values for the two time constants are calculated based on the ranges of values for the physical parameters (see the nomenclature table for the ranges).

The following range of values for the long and short time constants are produced:

$$T_L = 0.004 \text{ to } 0.2 \text{ sec} \quad (2.36)$$

$$T_S = 0.02 \text{ to } 0.4 \text{ msec} \quad (2.37)$$

The short time constant is not applicable because it represents an upper cutoff frequency far beyond the range of normal head movements. The cutoff frequency is calculated as the inverse of  $2\pi$  times the time constant, in this case a range of 0.4 to 7.9 kHz. Normal head movement is in the 0.1 to 5 Hz range (Wilson and Melvill Jones 1979). The long time constant represents a lower cutoff frequency that is consistent with physiologic data. The frequency range represented by the long time constants of Eq. 2.36 is 0.8 to 40 Hz. The cutoff frequency from the data in Fig. 2.7 is approximately 4 Hz, which falls within our calculated range. The implication for such small long time constants is that the mechanotransduction process is extremely rapid. Also, the smaller the long time constant, the bigger the range of frequencies, below the lower cutoff frequency, where the system acts as an accurate accelerometer with steady gain and zero phase angle.



## 2.6 TIME DOMAIN SOLUTIONS

With the availability of the simplified transfer function in Equations 32 and 33, analytic time domain solutions for various input stimuli can now be easily calculated. In this section, these time domain solutions from the approximated transfer function are compared with the time domain solutions from the original partial differential equation set. This is a further check of the validity of the approximate transfer function. The time domain response of the complete transfer function for a step change in skull velocity is found by solving the original partial differential equation set using a numerical finite difference approach (Grant and Cotton, 1990/91). The time domain solutions for the simplified transfer function are calculated using Matlab<sup>TM</sup> (The MathWorks, Inc.). All time response comparisons presented here utilize nondimensional variables. The solution to the simplified transfer function for a step change in skull velocity of magnitude  $V$  is:

$$\frac{\delta_0}{V} = \frac{1-R}{\left( M + \frac{1}{2}\sqrt{R} - \varepsilon \frac{1 + \frac{1}{2}\sqrt{R}}{M + \frac{1}{2}\sqrt{R}} \right)} \left( e^{-\left( \frac{\varepsilon}{M + \frac{1}{2}\sqrt{R}} \right) t} - e^{-\left( \frac{M + \frac{1}{2}\sqrt{R}}{1 + \frac{1}{2}\sqrt{R}} \right) t} \right) \quad (2.38)$$

This solution is plotted against the numerical solution of the partial differential equation set in Figures 2.8, 2.9, and 2.10. The magnitude of the step change in velocity for this

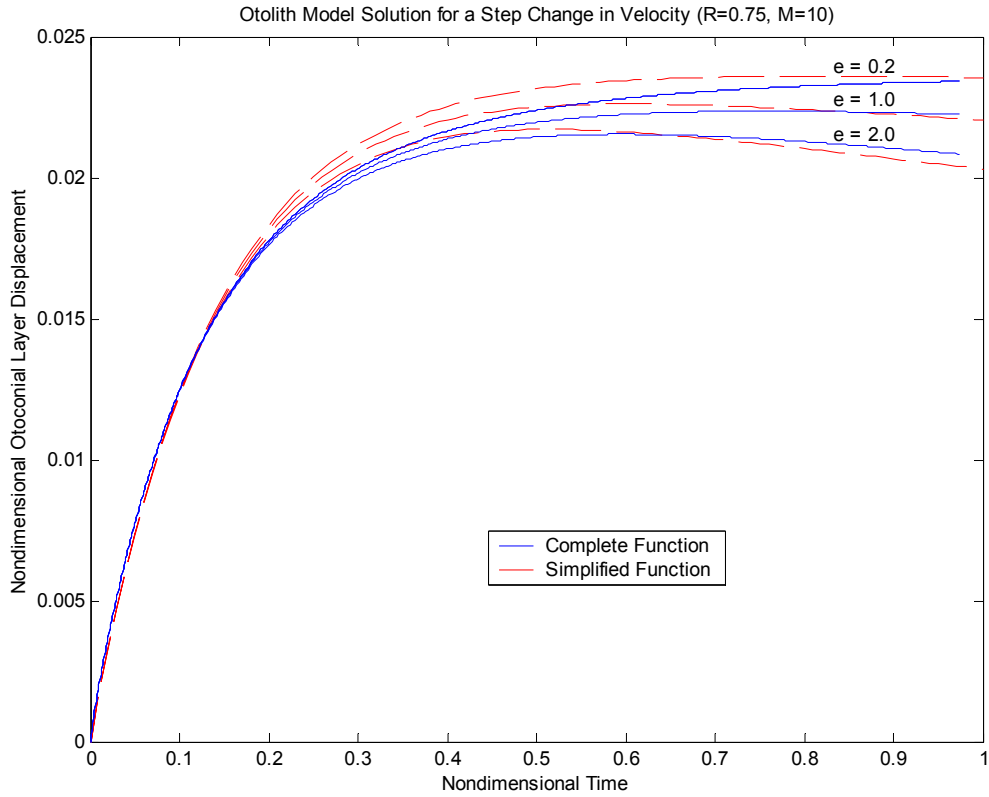


**Figure 2.8 – Time domain solutions of the complete transfer function and the approximate transfer function for a step change in skull velocity of magnitude one. The effects of varying  $\varepsilon$  are shown over the range  $\varepsilon=0.2$  to  $\varepsilon=2.0$ . The nondimensional variables  $R$  and  $M$  are held constant at 0.75 and 10 respectively. The complete transfer function was solved using a finite difference technique, while the approximate transfer function was solved using Matlab. For real time comparisons, 1 nondimensional time unit = 0.529 msec, where the following values were used for conversion:  $\mu_r=0.85\text{mPa sec}$ ,  $\rho_0=2.0 \text{ kg/m}^3$ ,  $b=15\mu\text{m}$ .**

comparison is one. In each of these figures, two of the three nondimensional parameters are fixed while the third is varied over its expected range of values. The nominal values for these parameters are  $\varepsilon = 0.2$ ,  $M = 10$ , and  $R = 0.75$ . The step change in velocity used as a stimulus here is actually an impulse in acceleration.

If the time axis is extended to 100 nondimensional time units for this calculation, the trend for the otoconial membrane to return to its initial position can be seen. The

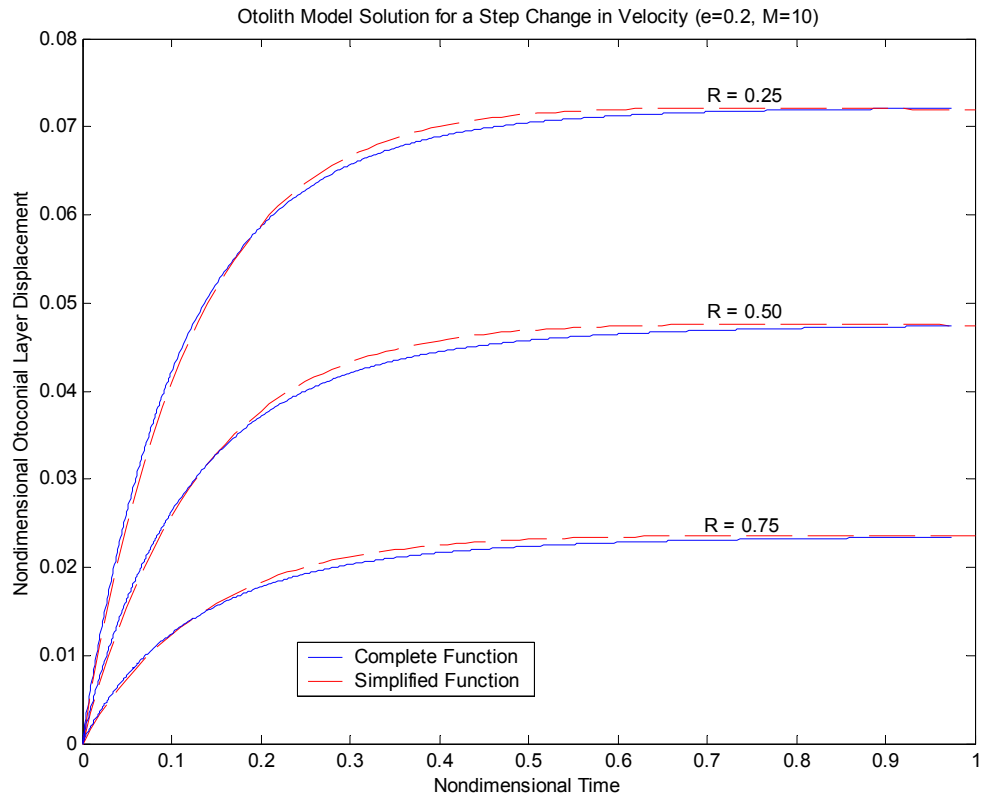


**Figure 2.9 – Time domain solutions of the complete transfer function and the approximate transfer function for a step change in skull velocity of magnitude one. The effects of varying  $R$  are shown over the range  $R=0.25$  to  $R=0.75$ . The nondimensional variables  $\varepsilon$  and  $M$  are held constant at 0.2 and 10 respectively. The complete transfer function was solved using a finite difference technique, while the approximate transfer function was solved using Matlab. For real time comparisons, 1 nondimensional time unit = 0.529 msec, where the following values were used for conversion:  $\mu_t=0.85\text{mPa sec}$ ,  $\rho_0=2.0 \text{ kg/m}^3$ ,  $b=15\mu\text{m}$ .**

approximate transfer function still does an excellent job of matching the finite difference solution. This information is presented in Figure 2.11.

As a further comparison, solutions for the case of a step change in acceleration are calculated. The time response solution of the approximate transfer function for a step

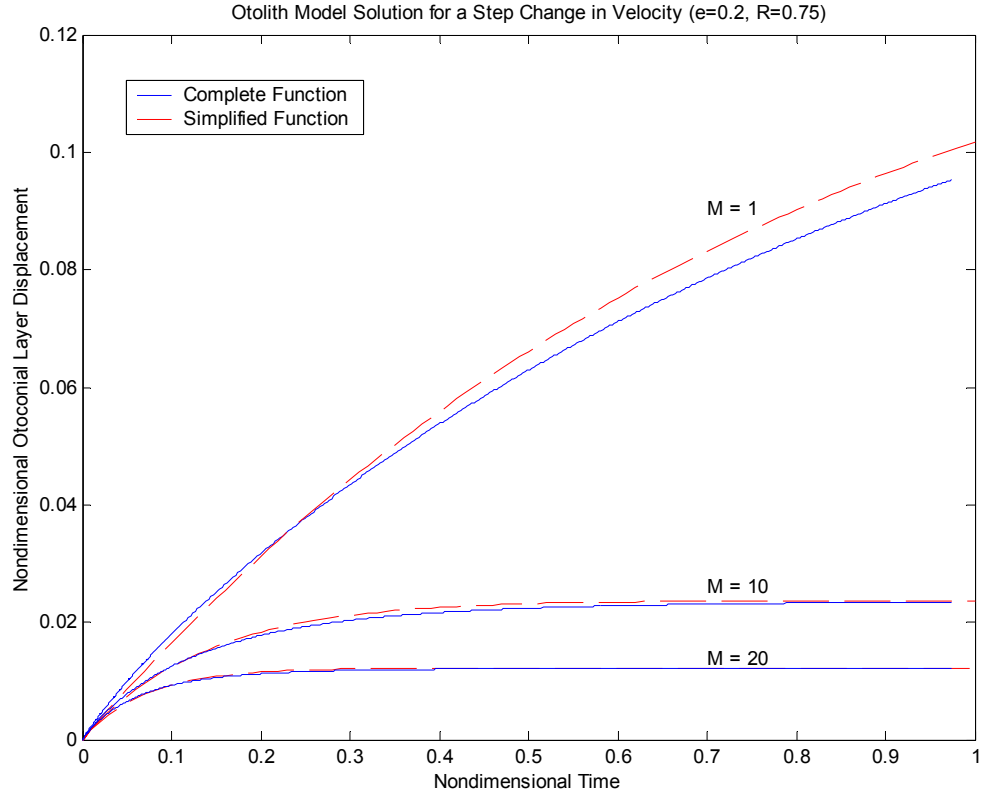


**Figure 2.10 – Time domain solutions of the complete transfer function and the approximate transfer function for a step change in skull velocity of magnitude one. The effects of varying  $M$  are shown over the range  $M=1$  to  $M=20$ . The nondimensional variables  $R$  and  $\varepsilon$  are held constant at 0.75 and 0.2 respectively. The complete transfer function was solved using a finite difference technique, while the approximate transfer function was solved using Matlab. For real time comparisons, 1 nondimensional time unit = 0.529 msec, where the following values were used for conversion:  $\mu_t=0.85\text{mPa sec}$ ,  $\rho_0=2.0 \text{ kg/m}^3$ ,  $b=15\mu\text{m}$ .**

change in acceleration of magnitude  $\bar{A}$  is:

$$\frac{\delta_0}{\bar{A}} = \frac{1-R}{\varepsilon} - \frac{1-R}{\left( M + \frac{1}{2}\sqrt{R} - \varepsilon \frac{1 + \frac{1}{2}\sqrt{R}}{M + \frac{1}{2}\sqrt{R}} \right)} \left[ \left( \frac{M + \frac{1}{2}\sqrt{R}}{\varepsilon} \right) e^{-\left( \frac{\varepsilon}{M + \frac{1}{2}\sqrt{R}} \right) t} - \left( \frac{1 + \frac{1}{2}\sqrt{R}}{M + \frac{1}{2}\sqrt{R}} \right) e^{-\left( \frac{M + \frac{1}{2}\sqrt{R}}{1 + \frac{1}{2}\sqrt{R}} \right) t} \right] \quad (2.27)$$

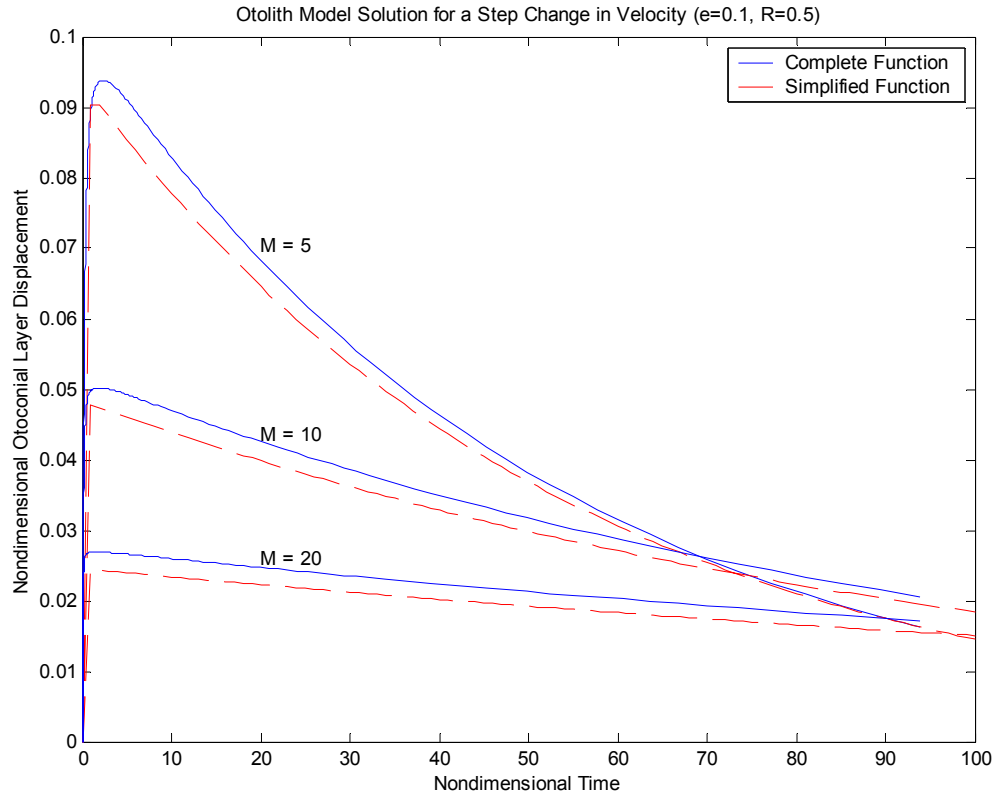


**Figure 2.11 – Solution for a step change in skull velocity (acceleration impulse) over a long time period. Here, the trend for the otoconial layer displacement to return to zero can be seen. The system damping, represented by  $M$ , affects the magnitude of the initial displacement and the time it takes for the otoconial layer to return to zero displacement. For real time comparisons 100 nondimensional time units= 52.9 msec, where the following values were used for conversion:  $\mu_r=0.85$  mPa sec,  $\rho_0=2.0$  kg/m<sup>3</sup>,  $b=15\mu\text{m}$ .**

Note that the constant displacement, reached at time equals infinity, predicted by this solution is a rather simple  $\delta_0 = [(1 - R)/\varepsilon]\bar{A}$ . The comparison of this approximate solution to the numerical finite difference solution for a step change in acceleration of magnitude one is shown in Figure 2.12.

When the system is subjected to a step change in acceleration stimulus, as opposed to a step change in velocity, a longer time elapses before maximum otoconial displacement is

reached. For this reason, the time scale in Figure 2.12 is extended to 250 nondimensional units or 132 msec, while the time scales in Figures 2.8, 2.9, and 2.10 show full deflection in about 1 nondimensional unit or 529  $\mu$ sec. It should be noted that the real times mentioned were calculated using typical mammalian values for the relevant physical parameters.

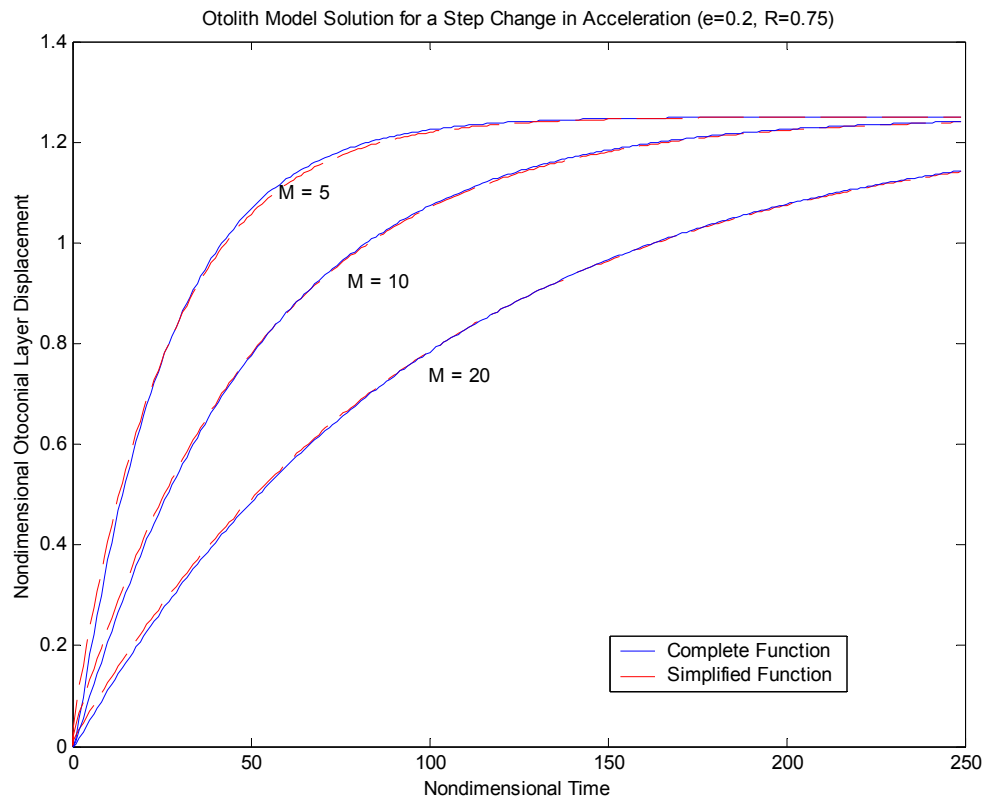


**Figure 2.12 – Solution for a step change in skull acceleration of magnitude 1. The system damping, represented by  $M$ , influences the time it takes for maximum displacement to be reached. For real time comparisons 100 nondimensional time units= 52.9 msec, where the following values were used for conversion:  $\mu_r=0.85$  mPa sec,  $\rho_0=2.0$  kg/m<sup>3</sup>,  $b=15\mu$ m.**

The comparisons presented in Figures 2.8 through 2.12 illustrate that time response results from the simplified transfer function are good approximations for the numerical finite difference solutions of the original partial differential equation set. There are some minor discrepancies at the outer limits of the ranges of the nondimensional parameters; however, all of the approximate solutions are within acceptable limits. Considering the complexity of the original partial differential equation set and its corresponding transfer function, the simplified lumped parameter model presented here, is a good representation of the actual time response.

## **2.7 DISCUSSION AND CONCLUSIONS**

The analysis presented here has produced a simplified mechanical transfer function that yields analytic time domain solutions for otoconial layer displacement. These simplified time domain solutions have proven to be a good approximation for the full finite difference solution to the original partial differential equation set. The derivation of the simplified TF is purely theoretical, however, its results correlate well with experimental frequency response data.

The time constants calculated from the simplified TF indicate that the dynamic response of the otolithic organs is extremely fast. The mechanotransduction process has a long time constant, which may range from 0.004 to 0.2 sec, and a short time constant in the 0.02 to 0.4 msec range. These time constants signify that the mechanical response to acceleration inputs and gravity direction changes during head tilt is extremely rapid.

With such a fast mechanical response, acceleration stimuli rapidly produce displacements of the otoconial layer that are proportional to the acceleration. For any second-order system to function as an effective accelerometer, it should be critically or slightly overdamped to prevent false output while the system is settling from a true acceleration input. In the case of the otoliths this settling would result in neural sensations of movement. It must also have a small long time constant for adequate dynamic response. The time constants calculated here are, therefore, appropriate for the otolithic organs. The frequency response match, of the simplified mechanical transfer function to physiologic data from first-order neuron recordings, indicates that the mechanoelectrical transduction and neural response are equally fast. Thus acceleration and gravity information is rapidly reported to the vestibular nuclei of the central nervous system. Such rapid response is probably required for normal animal locomotion on the earth.

The speed of the response of the otolithic organs to acceleration inputs makes it difficult to measure any dynamics of the end organ with perception or eye response techniques. Indeed, the time constants calculated in this work indicate that the information reported to the vestibular nuclei is much faster than the dynamics present in perception and eye response testing data (Denise, Darlot, Droulez, Cohen, and Berthoz, 1988; Paige, 1994). The time difference between the fast dynamics of the otolith organ response and the slower dynamics associated with perception and eye response is most likely introduced by the central nervous system. The slower dynamics of perception and eye motion indicate that there is probably considerable central nervous system processing of the otolithic organ signal.



The principle of equivalence in the general theory of relativity states that gravitational mass and inertial mass are equivalent. Thus it is impossible for a mass to distinguish the difference between gravitational attractive force and forces induced by acceleration. The otoliths are no different. Thus the central nervous system must evaluate otolithic signals and determine the difference between gravitational direction, which animals perceive as head pitch or roll, and linear accelerations. Central nervous system processing uses every sensory cue available in this determination. This complex process probably accounts for the slower dynamics of perception and eye motion. This intervening processing by the central nervous system probably makes experimental measurements of the otolith dynamic time constants, utilizing perception or eye motion, next to impossible.

The rapid response of the otolithic organs to changes in acceleration may be more accurately reflected in the neuromuscular system. This system must rapidly respond to postural changes during locomotion activities in order to keep a bipedal animal erect. Any testing that would be directed at measurement of the otolith organ system time constants would possibly be better pursued through measurement of the neuromuscular responses. Probably the best means of measuring the otolith time constants is through first order neuron data. This technique is unfortunately highly invasive and thus not suitable for human subjects.

The approximate dynamic transfer function developed here is the only lumped parameter model available that quantitatively describes utricle and saccule mechanical dynamic

function. This model has its origins in a more complex distributed parameter model but is simplified to an easily usable form that yields results comparable to the more complex model. The original goal in developing this simplification was to produce a simplified transfer function that could be used for modeling experiments in real time. This simplified model may also potentially be used to assess, in real-time, the effects of vestibular based non-lethal weapons. Additional uses of the model include developing otolith function tests and also tests to evaluate central nervous system response to otolith acceleration inputs.

## Chapter 3

# *A Two-Dimensional Finite Element Model for Analysis of Otolith Organ Deformation*

### 3.1 INTRODUCTION

The otolith organs, located within the inner ear, sense linear accelerations and transduce them into neural signals. Part of the vestibular system, these organs exist in pairs on each side of the skull – a left and right utricle and a left and right saccule. Anatomical studies have shown these organs to consist of a layer of mineral crystals, or otoconia, rigidly held together and coupled to sensory hair cells via a gelatinous interface (Fernandez, Goldberg, and Baird, 1990; Igarashi, 1966; Lindeman, Ades, and West 1970). The neural signal is generated when the hair cell cilia are deflected due to the shearing motion of the overlying otoconial membrane. In mammals the surface area of each organ is on the order of  $1 \text{ mm}^2$  and the number of sensory hair cells contained within the macula of each organ is on the order of 10,000 (Igarashi, 1966; Watanuki and Schuknecht, 1976).

Previous modeling efforts to describe otolith organ function have focused on mathematical descriptions of the otolith organ to predict its behavior (Kondrachuk and Sirenko, 1986; Grant and Best, 1987; Grant and Cotton, 1991; Benser, Issa, and Hudspeth, 1993). While these mathematical models have provided some insights, their results have limitations. By necessity, when constructing such analytical models the complex geometry of the structure must be approximated by a mathematical simplification. Finite element modeling, however, uses the very geometry of the structure to set up the system of equations that are used to predict organ behavior. While the finite element method of modeling is rooted in mathematics and can return numeric results, it has the added benefit of presenting a visual analysis of organ response to a stimulus. In this chapter a simplified two-dimensional finite element model of an otolith organ is presented. The structure of the organ, in this case the utricular macula, is represented as a collection of finite elements. Each element has appropriate physical properties, e.g. - density, assigned to it depending upon its position in the structure. An in-depth knowledge of utricular anatomy is obviously required, but unfortunately not readily available. For this reason, some features and values in the model have to be estimated.

The objective of this work is to produce a model that characterizes the deformation of the organ under an acceleration stimulus and more importantly, predicts the deflection of the sensory hair cell cilia bundles within the organ. It is important to note that this two dimensional model is a purely elastic approximation of an otolith organ. It does not include either the fluid damping that occurs *in vivo* by the endolymph fluid surrounding

the organ or the viscous damping of the gel layer. The viscous damping effects of the endolymph and the gel layer would not appreciably affect the values of the natural frequencies and mode shapes calculated by the model, however, they would reduce the absolute amplitude of the model displacement. Follow-on work to determine the effects of damping on the otolith model is planned.

## **3.2 BACKGROUND**

### ***3.2.1 Finite Element Modeling***

Finite element modeling was developed in the 1960s to solve structural engineering equations of elasticity and is used extensively in the fields of civil and mechanical engineering. Further developments in modeling techniques extended the original work in structures to solve problems in the area of fluid mechanics (Cook, Malkus, and Plesha, 1989; Reddy, 1993). Finite element modeling has also been applied in the field of biomedical sciences to model skeletal stresses, joint prostheses, and blood flow among other things (Gilbertson, Goel, Kong, and Clausen, 1995; Huiskes and Chao, 1983; Park, Dujovny, Park, and Diaz, 2001; Yin, 1985).

The use of finite element modeling in vestibular mechanics has been extremely limited, with emphasis in three areas: otolith organ modeling (see references in the following paragraphs), semicircular canal modeling (Njeugna, Eichorn, Kopp, and Harlicot, 1992; Hughes, McGrath, McGrath, and Rupert, 2001) and hair cell stereocilia bundle modeling

(Duncan and Grant, 1997; Cotton and Grant, 2000). Of particular interest to the current research is otolith organ modeling.

Twizell and Curran (1977) were the first to apply finite element modeling to the vestibular system. They developed a two-dimensional finite element model of the otolith membrane. They found that the finite element model allowed the complex boundary shape of the organ to be incorporated into the solution. This produced results that more closely resembled experimental findings (Lowenstein and Roberts, 1950) than results from other computational methods (Hudetz, 1973).

Ferreira, Grant, and Peterson (1996) developed a two-dimensional finite element model of a cross section of an otolith organ. Methods used in and results from this model are presented in the current chapter.

Kondrachuk (2000) developed a simplified three-dimensional finite element model to simulate the bullfrog experiment performed by Benser (1993). In the Benser experiment, the otoconial layer was removed and a glass probe was coupled to the top of the gel layer. A known force was applied to the probe and resulting gel layer displacements measured. The finite element model was a simple rectangular model of the organ with force applied as in the experiment. Kondrachuk found that a homogenous gel layer was insufficient to duplicate experimental results, and adding a less stiff sub-layer was necessary.

Expanding on the work of Ferreira *et al.* (1996) and his own earlier model (Kondrachuk, 2000), Kondrachuk (2001) developed a three-dimensional guinea pig utricular otolith finite element model that incorporated the anatomically correct boundary shape of the organ. The key findings from this modeling effort were that the gel layer must have a sub-layer with a much smaller Young's modulus, the organ boundary plays a role in organ function, and that changes in endolymphatic pressure may deform the otolith membrane.

These various finite element modeling efforts over the past 25 years have shown that finite element modeling is a powerful tool for investigating the structure and function of the vestibular system.

### **3.2.2 Otolith Organ Morphology**

To produce an accurate finite element model a good understanding of the morphology and physical properties of the structure being modeled is necessary. As illustrated in Figure 3.1, each otolith organ is composed of three layers - an otoconial layer with two gel layers beneath it.

Although not flat, as seen in Figure 3.2, these layers in the utricle are in a roughly horizontal orientation, while in the saccule the orientation is more nearly vertical (Curthoys and Oman, 1987; Kelly, 1991).

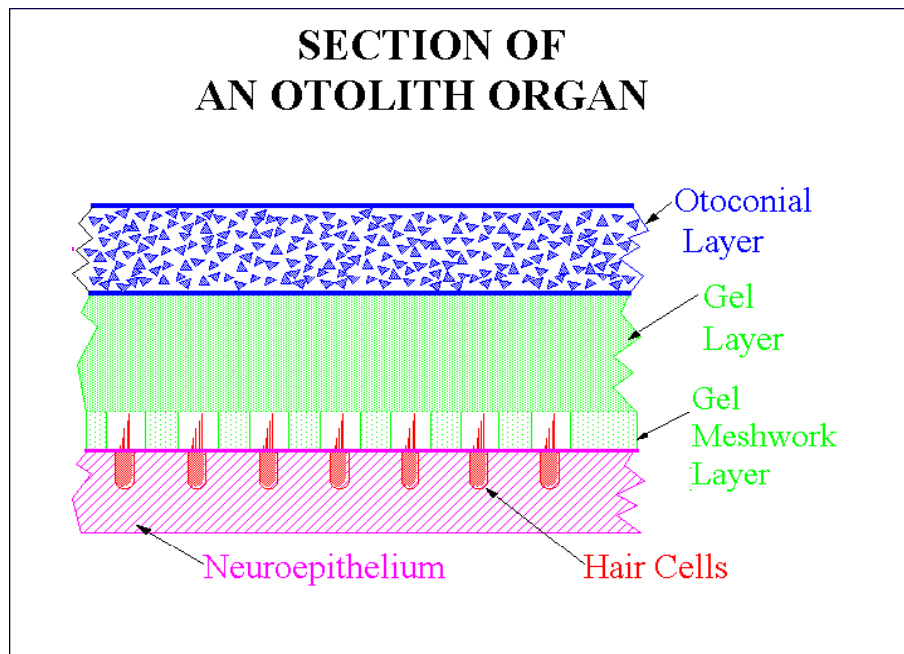


**Figure 3.1 - Section of an otolith organ showing its layered structure.**

The uppermost layer is known as the otoconial layer or membrane. It is composed of calcite crystals, or otoconia, supported in a gel matrix. This layer comprises the mass of the organ. The size and shape of the otoconial crystals varies from species to species and within each organ, depending upon position in the organ. In mammals, the dimensions of the otoconial crystals are on the order of 10 microns (Carlstrom, 1963).

The middle layer is commonly referred to as the gel layer. It is an isotropic mucopolysaccharide gelatinous material consisting of randomly oriented filaments. It serves as an interface between the otoconial layer and the ciliary bundles of the sensory hair cells, and is sometimes thought of as a support structure for the otoconial mass. This layer adds elastic damping to the system.



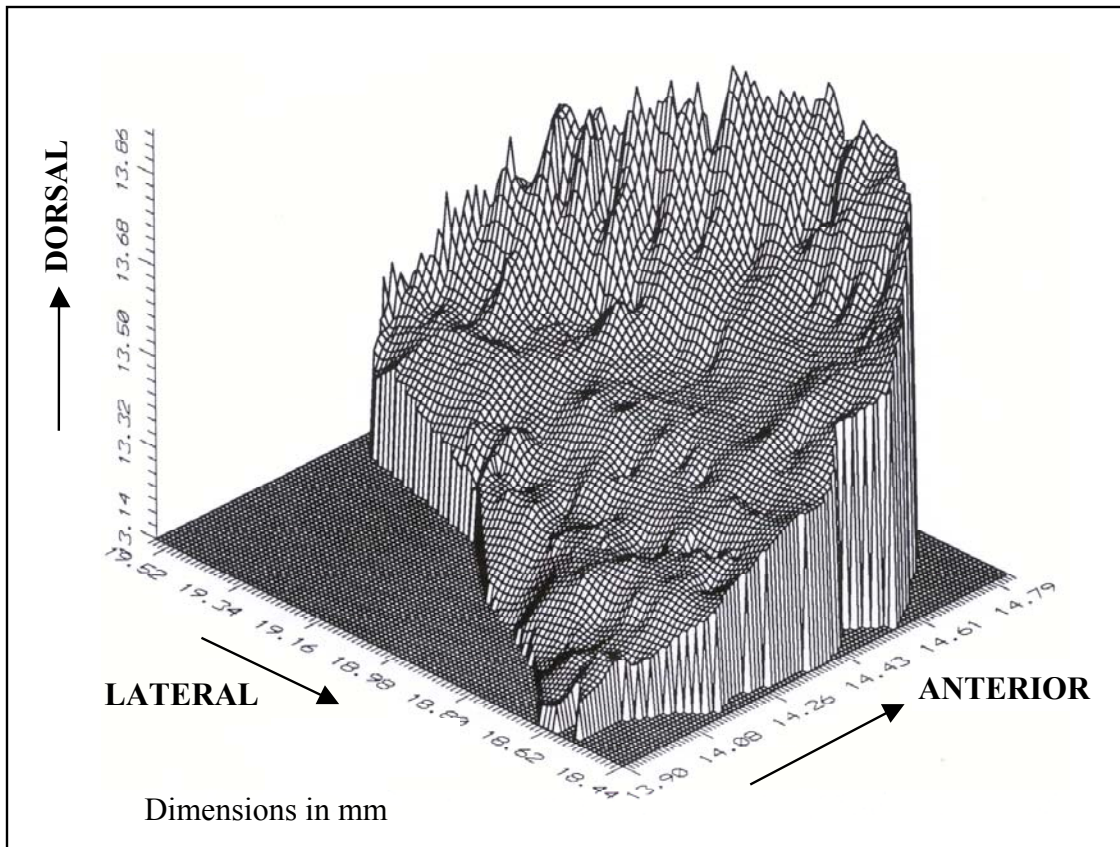


**Figure 3.2 - Topographic study of a guinea pig right utricle macula showing its cupped nature. The axes are parallel to the stereotaxic coordinate axes since the data points were gathered in the guinea pig stereotaxic coordinate system. (from Curthoys 1996).**

The lowest layer, connecting the gel layer with the sensory epithelium, is a less dense version of the gel layer. In the bullfrog, the structure of this layer is anisotropic, consisting of longitudinally oriented filaments and is known as the columnar filament layer (Kachar, Parakkal, and Fex, 1990). In mammals, this layer, the gel meshwork, consists of randomly oriented filaments as in the gel layer (Lindeman *et al.*, 1970). Whether the strands are oriented or random, anatomical studies agree that this layer is attached only to the gel layer and the sensory epithelium and not to the hair cell bundles. The ciliary bundles protrude through spaces in the gel meshwork. The kinocilium, or

longest cilium, of each hair cell is attached to the gel layer such that movement of the gel layer in turn moves the kinocilium. Links between the kinocilium and each stereocilium cause the entire ciliary bundle to be deflected when organ deformation is initiated by movement of the otoconial mass. The sensory epithelium, where the bodies of the hair cells reside, can be considered to be rigidly attached to the skull.

Each organ is located within a fully enclosed, fluid-filled duct. The endolymph fluid surrounding the organs has a specific gravity similar to that of the gel layers. This fluid immersion results in a buoyant effect on the organ. As a result, the gel and gel-meshwork layers are essentially isolated from responding to acceleration stimulus and any gel deformation is the result of otoconial layer movement.

From a planar perspective, each organ is divided into three zones (see Figure 3.3). A central zone, called the striola, runs parallel to the longest axis of each organ. In both the utricle and saccule this axis is roughly anterior-posterior in orientation. The other two areas are the zones on either side of the striola. In the utricle these are the medial and lateral zones, in the saccule they are the superior and inferior zones (Spoendlin, 1965; Jongkees 1967). The size of the calcite crystals in the otoconial layers, the type and orientation of hair cells, are important variables in each area.

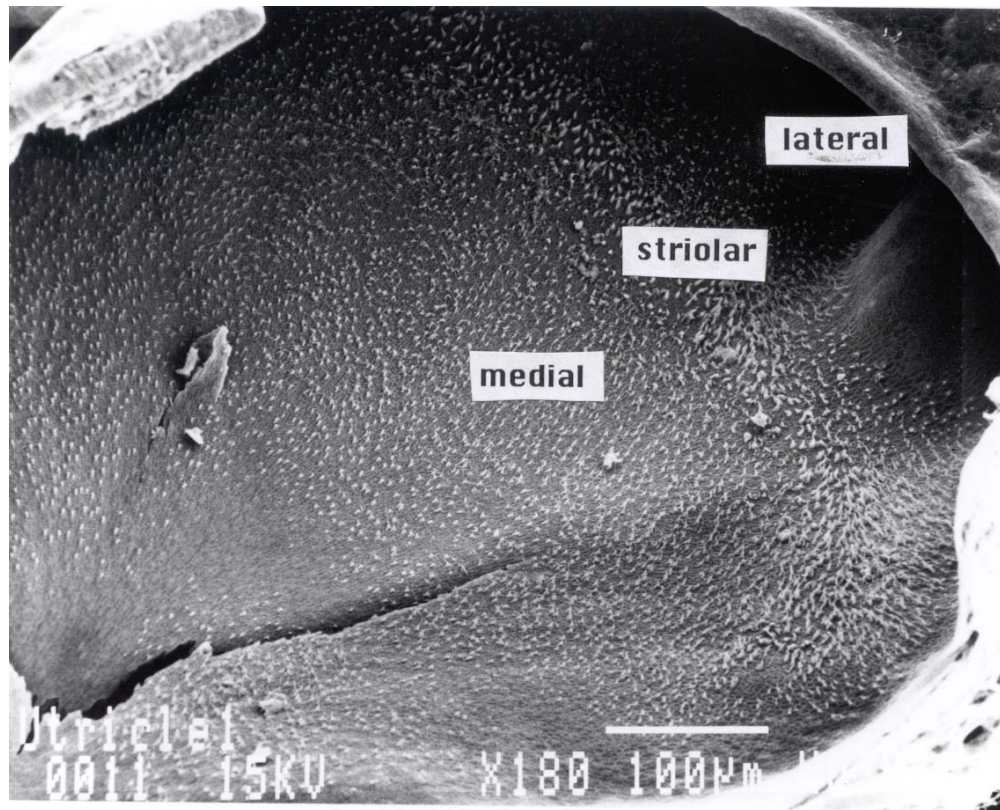


**Figure 3.3 - Turtle utricular macula showing striolar, medial, and lateral zones. The otoconial and gel layers have been removed, exposing the neuroepithelium and hair cell ciliary bundles (from Peterson 1996).**

### ***3.2.3 Displacement of Otolithic Membranes Deflects Hair Bundles***

The otolithic membranes are deflected when an acceleration stimulus is applied to the skull as illustrated in Figure 3.4. In a static situation, e.g.- the skull is at rest but tilted, the otoconia are displaced relative to the skull. This is due to the acceleration of gravity acting on the mass of the otoconial crystals. The resulting displacement of the crystals is in the same direction as the gravitational field. In a dynamic situation, e.g.- forward linear acceleration in an automobile, the motion of the otoconia lags the motion of the skull. As the skull is accelerated forward, the otoconia of the horizontally oriented

utricle take longer to accelerate due to their elastic attachment to the skull. As a result, the direction of otoconial displacement is opposite the direction of acceleration of the skull. Displacement of the otoconial mass relative to the skull deforms the gel and gel meshwork layers. These intermediate layers experience a shear deflection under an acceleration stimulus. As previously described, kinocilial attachment to the gel layer causes hair bundle deflection when there is movement of the otoconial layer.

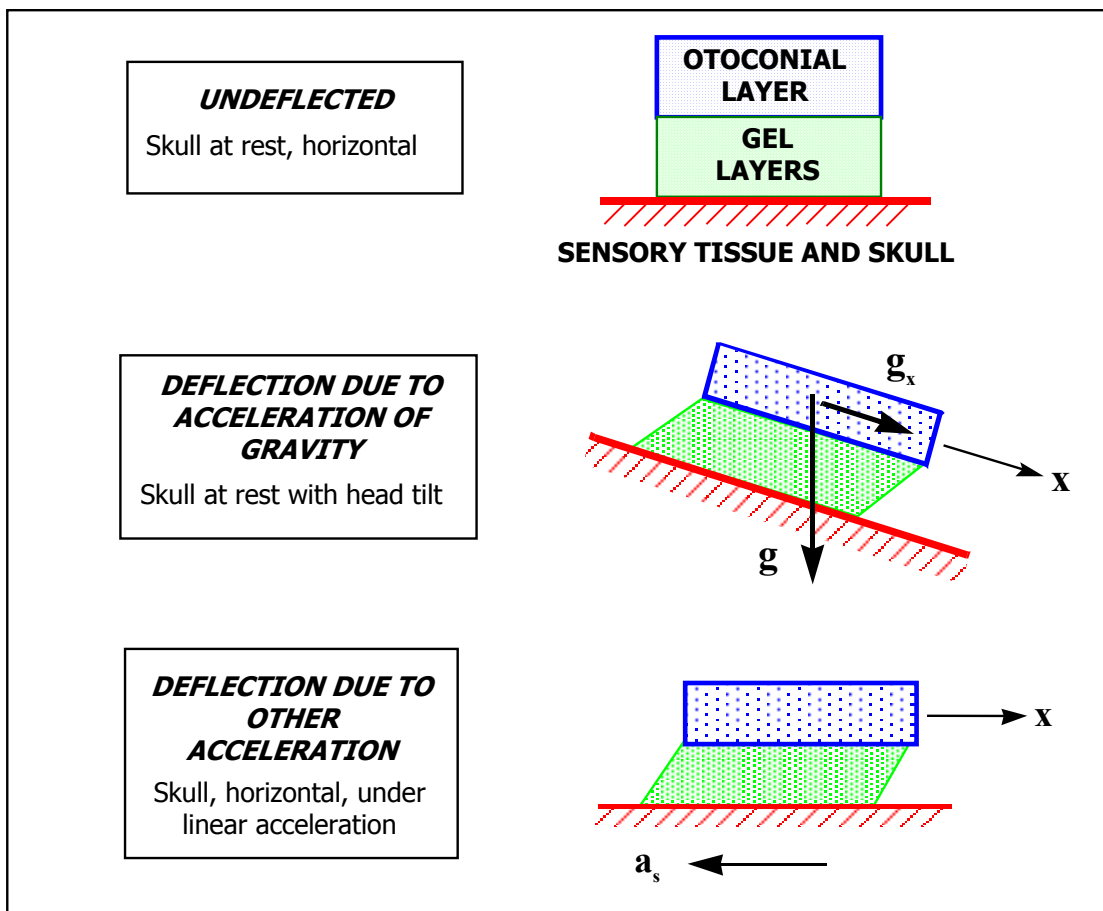


Figure 3.4 – Otoconial layer displacement due to acceleration.

### 3.2.4 Ciliary Bundle Deflection Initiates a Neural Signal

Deflecting the ciliary bundle affects ion channels into the cell and, depending on the direction of deformation, may cause the cell to either depolarize or hyperpolarize. There appear to be numerous ion channels that remain open when the hair cell is at rest with the ciliary bundle undeflected. A deflection of the ciliary bundle toward the kinocilium causes additional channels to open, depolarizing the cell, and putting it more ionically in balance with the surrounding endolymph. A deflection of the ciliary bundle away from the kinocilium closes the channels that are open at rest, interrupting the steady-state ion flux, and hyperpolarizing the cell. The locations and gating mechanisms of these

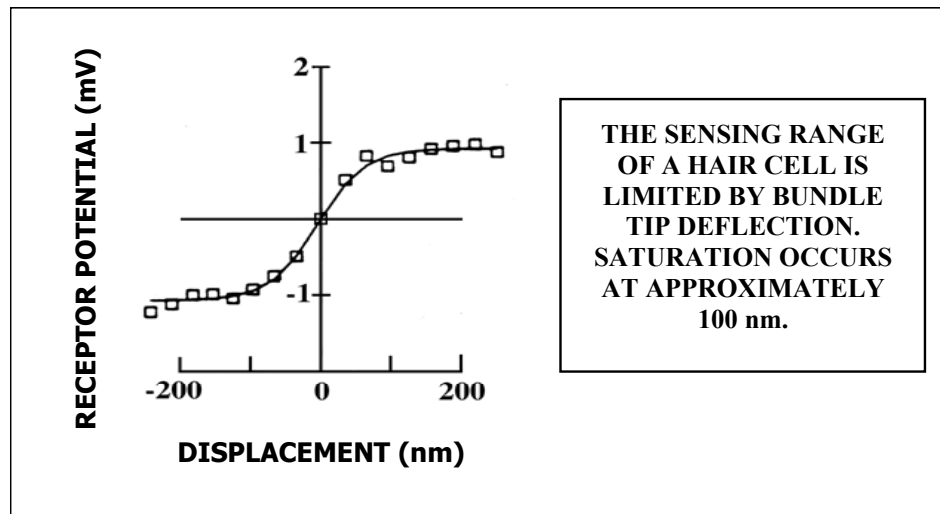


Figure 3.5 – Hair cell depolarization versus ciliary bundle deflection (Reprinted from Howard and Hudspeth 1988, with permission from Elsevier).

channels are unknown. Depolarization and hyperpolarization occur only over a limited range of deflections as seen in Figure 3.5 (Howard and Hudspeth, 1988; Hudspeth, 1989).

Different values for ciliary bundle stiffness,  $k$ , have been measured experimentally. Some values are shown in Table 3.1. Stiffness controls the amount of deflection,  $d$ , for a given force,  $F$ , on the bundle:

$$d = F/k \quad (3.1)$$

**Table 3.1 - Different hair cell bundle stiffness values.**

<i>INVESTIGATOR</i>	<i>STIFFNESS</i> <i>(<math>10^{-4}</math> N/M)</i>	<i>HAIR CELL ORGAN</i>
Ashmore (1983)	1.32	Frog Sacculus
Howard and Ashmore (1986)	2.56	Frog Sacculus
Howard and Hudspeth (1988)	6.3	Bullfrog Sacculus
Denk, Webb, and Hudspeth (1989)	3.41	Frog Sacculus
Strelioff and Flock (1984)	1 – 97.2	Guinea Pig Cochlea

There are several distinct types of hair cells within each macula. The differences can be seen in the sizes and arrangements of the hair cells' ciliary bundles, as well as in the types of cellular innervation (Fernandez *et al.*, 1990; Lindeman *et al.*, 1970). Since this model deals with structural deformation, the important difference is in the hair bundle. Different bundle morphologies exist in different areas of the otolith organs; see Figure 3.6. These morphologic variations may correlate with variations in bundle stiffness. To date, experimental measurement of hair bundle stiffness has been limited by the measurement techniques available. Furthermore, only certain regions of the organ are accessible and hence only certain types of hair cells have been measured.

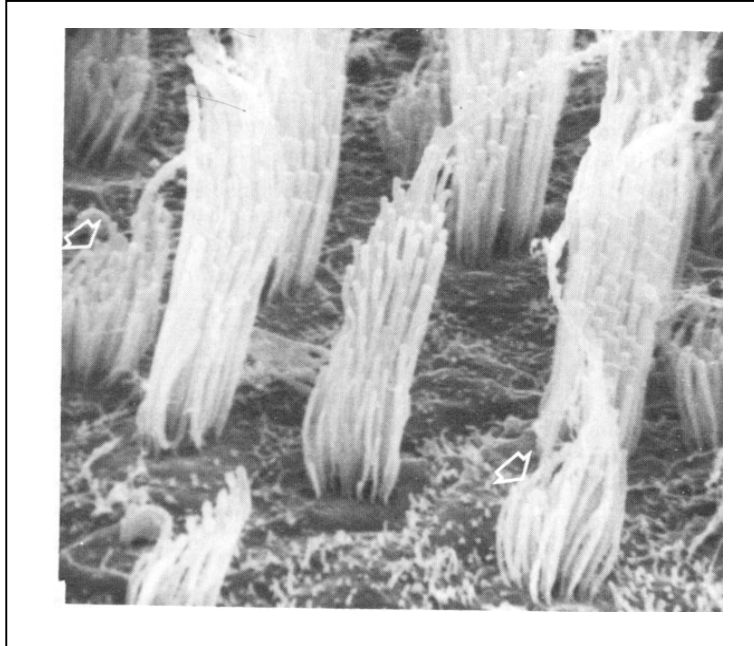


**Figure 3.6 – Scanning micrograph showing variations in hair bundle morphology on the macula utriculi of the chinchilla (magnification 4650). Note the shorter stereocilia of the two bundles marked by arrows, which may contribute to morphologic stiffness variations. (from Lindeman *et al.*, 1970).**

### **3.3 THE MODEL**

#### ***3.3.1 Finite Element Representation of Otolithic Organs***

The finite element model presented here is a two dimensional representation of an otolith organ section based primarily on mammalian anatomical studies. In the development of a finite element model the following parameters are required: shape and dimensions, material properties, boundary conditions, and loads. As described previously, the otolith organ consists of four separate parts: an otoconial layer, a gel layer, a gel meshwork layer, and hair cells that are rooted in the neuroepithelium. To produce the finite element

model it was necessary to obtain, or estimate, the parameters for each part of the otolith organ. Dimensions for the model were taken from detailed anatomic studies of mammalian otolithic organs. A photomicrograph from one of these studies performed on a squirrel monkey, Igarashi (1966), is presented in Figure 3.7. This photo shows the layered structure of the organ, along with a schematic diagram giving some dimensional data. A second study, Fernandez et al (1990), presents similar data from a chinchilla macula utriculus. Dimensions of the monkey layers are remarkably similar to those of the chinchilla, which supports generalizing the finite element model as a mammalian model.

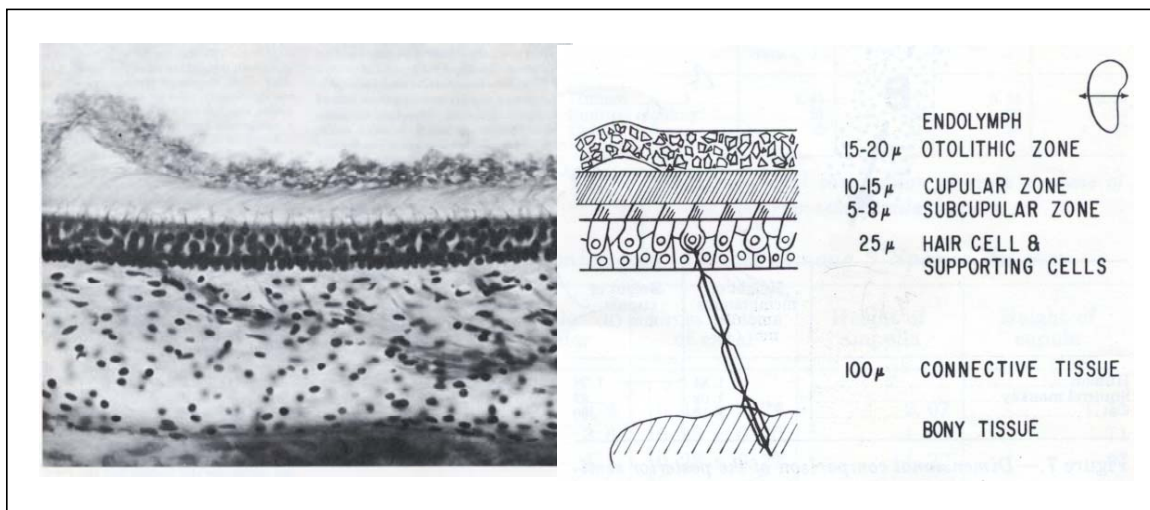


**Figure 3.7 – A high magnification photo of a section through a macula sacculi from a squirrel monkey. The schematic defines the layers and their dimensions. The cupular and subcupular zones are the gel and gel meshwork layers respectively (from Igarashi, 1966).**

The finite element model is shown in Figure 3.8. Each layer of the organ has been modeled separately so that properties could be correctly assigned.



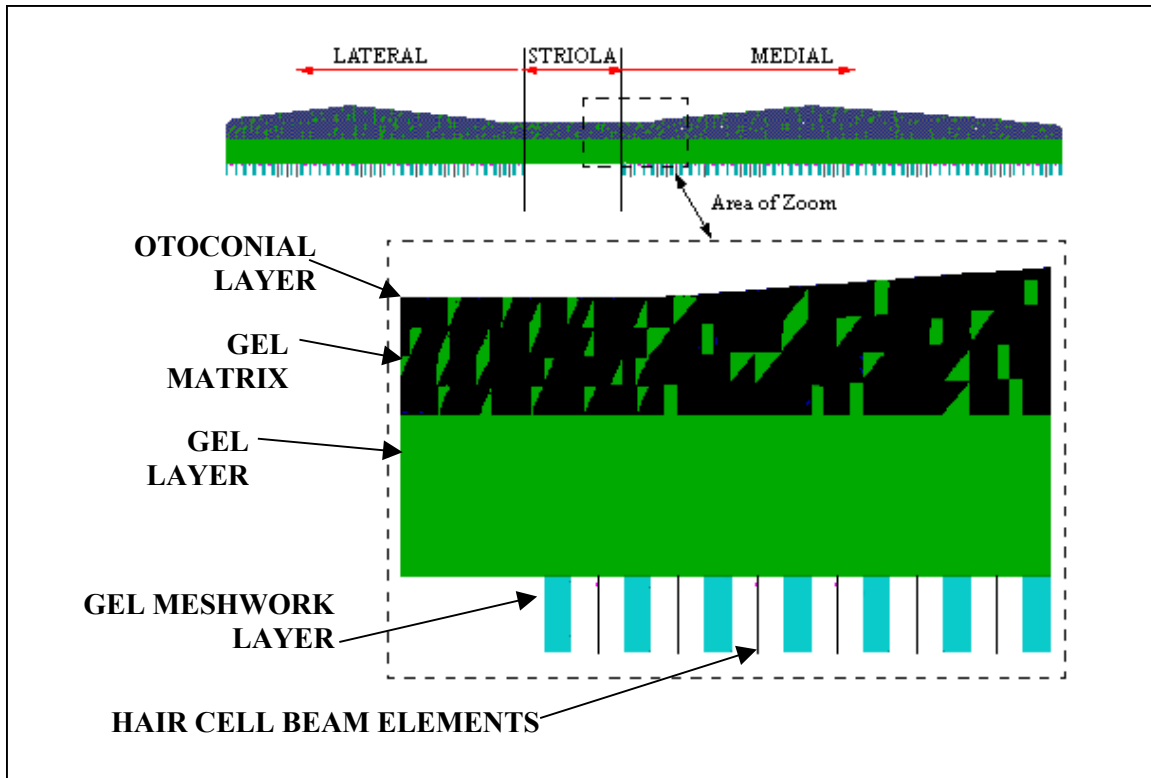


**Figure 3.8 - Finite element representation of a section through a mammalian utricular macula.**

### **Otoconial Layer**

The calcite crystal / gel matrix is modeled as a combination of plate elements with either calcite or gel properties. The plate elements chosen are three node triangular plates, which are used extensively in finite element methods. Their behavior is well understood. These elements provide accurate, stable results over a wide range of boundary conditions and loads (Cook *et al.*, 1989; Reddy, 1993).

The crystal packing density is estimated from photomicrographs such as those previously presented, which show that the density of the crystal is greatest near the center, or striolar region

### **Gel Layer & Gel Meshwork Layer**

The gel layer is modeled as an homogenous layer of four node quadrilateral plate elements. Like the triangular elements used in the otoconial layer, these quadrilateral elements are well behaved. The gel meshwork layer is also modeled with four node quadrilateral plate elements. The meshwork layer is not continuous, however, but alternates with hair cell beam elements

### **Hair Cells as Cantilevers**

Each hair cell bundle is modeled as a single cantilevered rod having a stiffness equivalent to the entire bundle. This approach for modeling hair cells was chosen because testing for bundle stiffness has shown that the hair bundles deflect in the manner of a cantilever beam rather than a hinged or pinned beam. In typical experimental testing of hair bundle stiffness, the cell body is held in a fixture while a glass fiber applies a measured load to the tip of the kinocilium (Howard and Hudspeth, 1988). This is the approximate location at which the kinocilium would be attached to the gel layer *in vivo*. Alternatively, the gel layer may be removed from the organ and the organ itself held fixed while the hair bundle is deflected (Barrett, 1995; Barrett, Peterson, and Grant, 1999). These types of deflections, analogous to normal physiologic deflections, show bending of the hairs and

not a simple rotation about the cell-fixed end (Ohmori, 1987). The kinocilial attachment to the gel layer is modeled as a simple pinned junction.

### ***3.3.2 Assigning Material Properties***

The shape and dimensions of the otolith organ are documented in the literature as shown in the previous section; however, the material properties are not as well understood. Finite element models require as input the modulus of elasticity and the density for each element in the model. Values for three of these parameters are published in the literature: the density and elastic modulus of the otoconia and the modulus of elasticity, or stiffness, of the hair cell ciliary bundles. The other parameters were estimated, as described below, or eliminated. To eliminate three of the parameters, namely: the densities of the gel layer, gel meshwork layer, and hair bundles, these elements were all considered massless. This assumption is valid for modeling purposes because the otoconial layer is much denser than any known mucopolysaccharide gel, such as those comprising the gel and gel meshwork layers.

#### **Published Values**

The calcite crystals that comprise the otoconia are well characterized, calcite being one of the most commonly occurring minerals on earth. Its modulus of elasticity is 72 GPa and its density is 2.71 g/cm<sup>3</sup> (Almaz, 2001). Experimentally obtained values for hair cell stiffness documented in the literature are presented in Table 3.1 and range from 0.0001 to 0.01 N/m. For the results shown in Fig. 3.9 a value of  $k=3.4 \times 10^{-4}$  N/m was used.

### **Estimated Values**

The moduli of elasticity for the gel layer and the gel meshwork layer were estimated; experimental data for these values are not available. The following requirements were imposed when estimating values:

- The otoconial layer modulus must be much greater than gel layer modulus. The calcite crystals of the otoconial layer are rigid in contrast to the deformable mucopolysaccharide gel of the gel layer and hence must have a much greater elastic modulus.
- The value for the gel layer modulus must produce deflections of the otoconial layer within normal physiological boundaries.

With these two constraints, the gel layer modulus was estimated to be 10 Pa.

- The gel meshwork layer modulus must be less than gel layer modulus. These two gel layers consist of the same material but the meshwork layer is less dense than the gel layer and must therefore have a lower modulus of elasticity.

Using this criterion, the gel meshwork layer elastic modulus was estimated to be 1 Pa.

### **3.3.3 *Boundary Conditions***

The boundary conditions used for the model are estimated based on the known anatomy and physiology of the otolith organ. The three layers are assumed to be attached to each other with no slippage of adjacent plates. As mentioned previously, the hair cell beam elements are cantilevered out from the neuroepithelium and have simple hinged connections to the gel layer. The entire structure is anchored to the neuroepithelium through the plate elements of the columnar filament layer. The elements in contact with the neuroepithelium are fixed along their bottom edges.

## **3.4 RESULTS**

### **3.4.1 *Results for Deformation Due to Acceleration***

A 1g load (acceleration stimulus of 1 x the acceleration of gravity), acting in the horizontal direction indicated in Figure 3.9, is applied to the otolith model. The results of the analysis are shown in Figure 3.9 with the deformed or deflected state of the otolith model shown at the top of the figure, and a graph indicating the numeric value of hair bundle tip deflection depicted at the bottom. The deformed shape of the otolith model is reasonably uniform across the cross-section of the otolith with the greatest hair cell bundle deflection occurring at the tip of the hair cell bundle.

The graph of hair bundle tip deflection shows a variation in hair bundle deflection in two separate but related areas. The first variation in hair bundle deflection is small and occurs due to edge effects at the lateral and medial borders. These edge effects are minor and would be expected from the anatomy of the otolithitic organs. The second variation in hair bundle deflection is large and occurs near the striolar region.

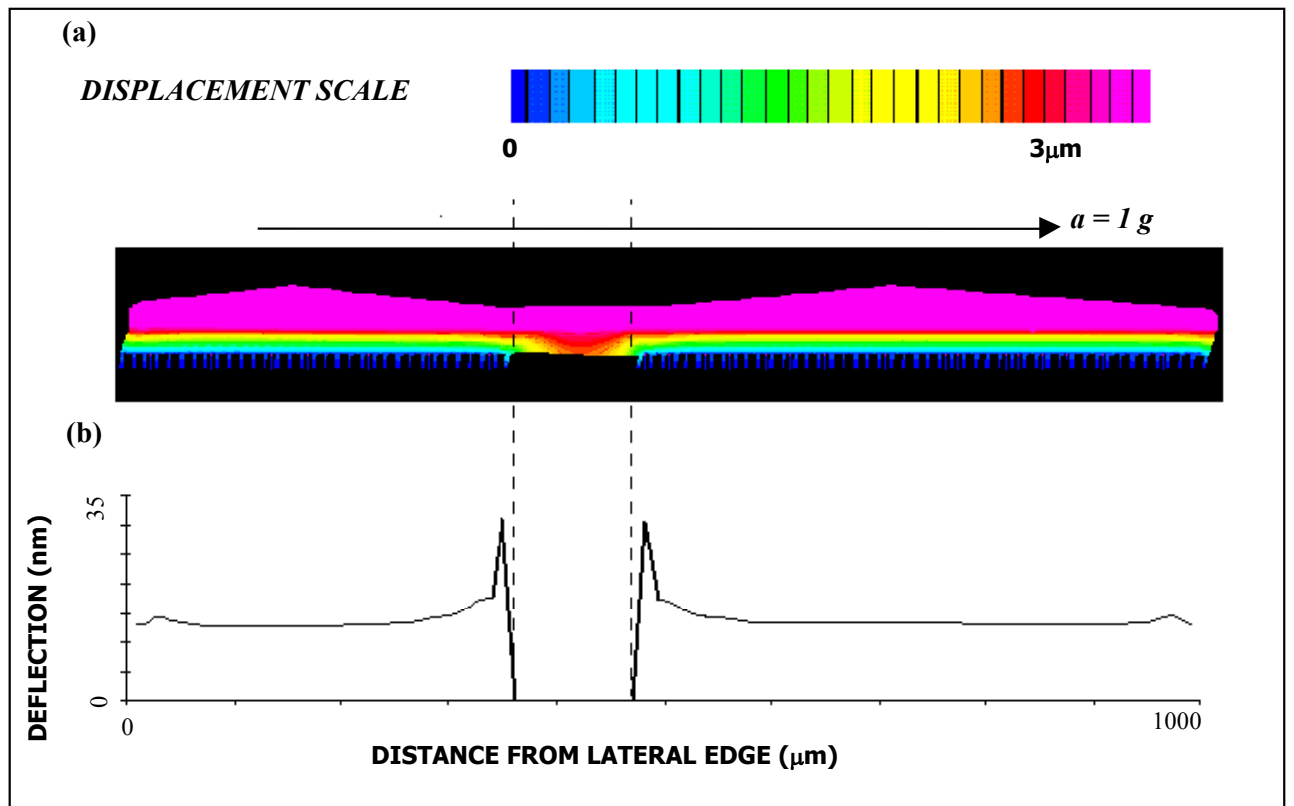


**Figure 3.9 – (a)Contour plot showing otolith organ deformation under a 1g load. (b)Graph showing variation in bundle tip deflection over the surface of the sensory epithelium.**

This major variation in hair bundle deflection and subsequent reduction to zero at the striolar region is caused by assuming there is no hair cell/gel layer attachment at the striola. This result is unexpected and raises questions about the validity of the assumption of unattached hair cells in the striolar region.

### 3.4.2 Results for Variation in Hair Bundle Stiffness

Published values of hair bundle stiffness range over two orders of magnitude. The actual range of stiffness may be even greater. Varying the value of hair cell bundle stiffness in the model results in different tip deflections for a given acceleration stimulus. In order for the hair cell to sense the acceleration accurately, its cilia bundle tip deflection must be within a certain sensing range. This range of sensitivity was measured by Howard (1988) to be between 2 and 100 nm (Figure 3.5). For a given value of bundle stiffness,  $k$ , varying the acceleration stimulus over the entire range of human perception resulted in tip deflections outside of the hair cell range of sensitivity. In order for the tip deflections to be within the sensing range, over the perception range of .005g to 25g, it was necessary to vary the bundle stiffness as well. This concept is illustrated in Figure 3.10.

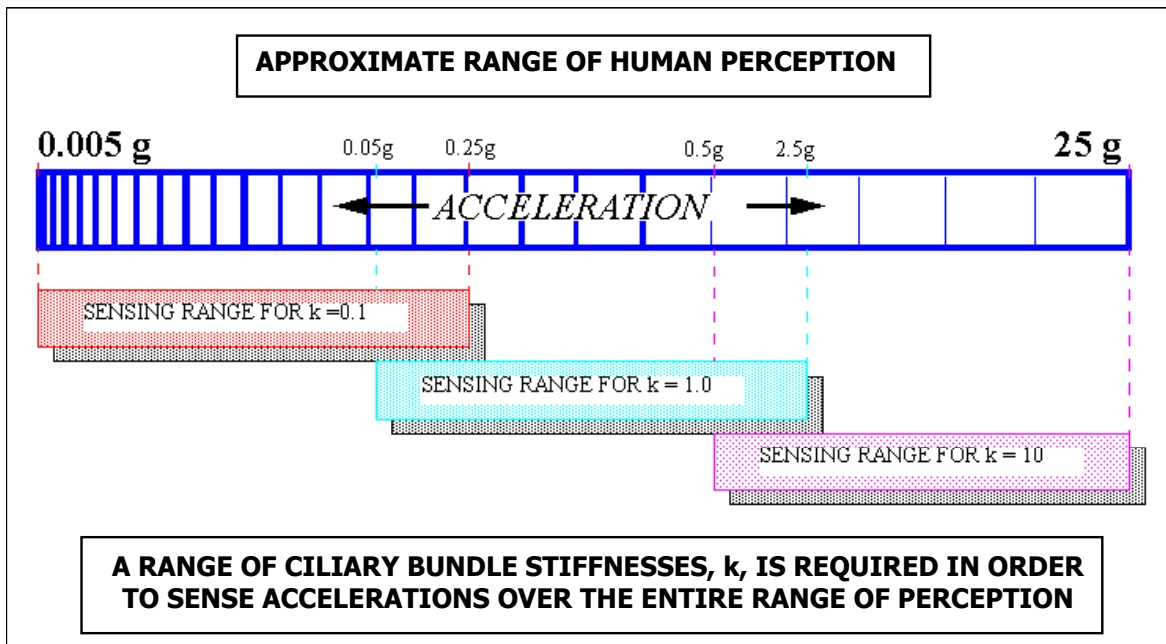
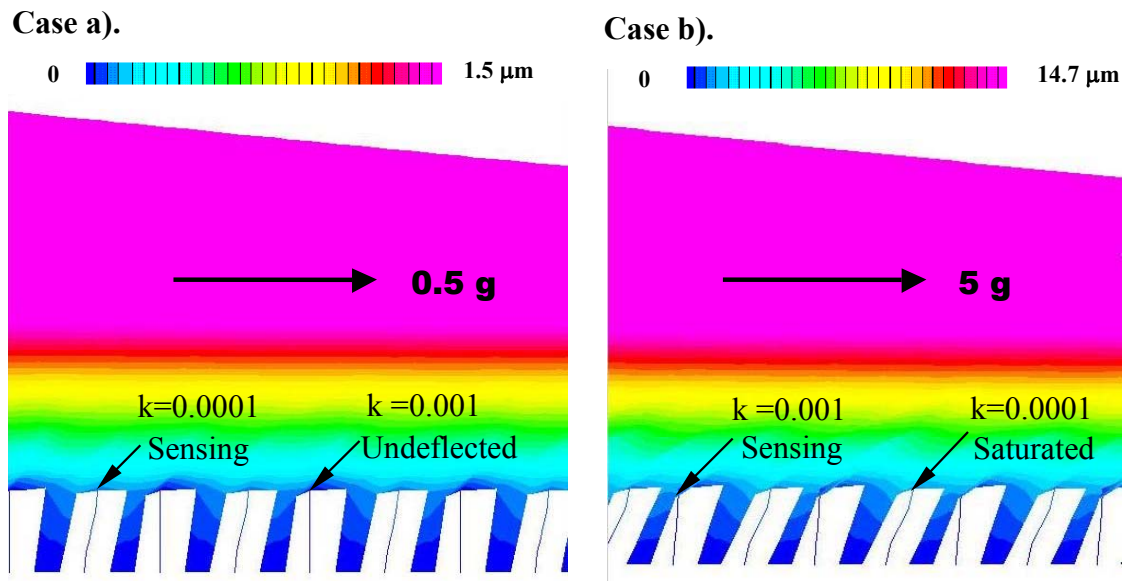


Figure 3.10 - Range of human acceleration perception and the necessary bundle stiffness variation predicted by the model to accommodate this range (hair bundle stiffness,  $k$ , is  $\times 10^{-4}$  N/m).

As a further illustration of this point, the model was configured with hair cell bundles of alternating stiffness. The values used were  $k=0.0001$  and  $k=0.001$  N/m. Two different load cases were then applied to the model. The first case, a 0.5g load, resulted in deflecting the less stiff bundle tips to within their sensing range. The stiffer bundles, however, were left undeflected. The second case, a 5g load, resulted in saturating the less stiff hair cell bundles while deflecting the stiffer bundles to within their sensing range. See Figure 3.11.



**Figure 3.11 – Model configured with hair cell bundles of alternating stiffness values (the units for  $k$  are N/m). In case a), a 0.5g load is sensed by the less stiff bundles while the stiffer bundles are undeflected. In case b), a 5g load saturates the less stiff bundles while being sensed by the stiffer bundles.**



### **3.4.3 *Natural Frequencies and Mode Shapes***

The model predicts natural frequencies of oscillation for the otolith organ and also provides visual images of the organ in its deformed state. The first four frequencies are: 280 Hz, 850 Hz, 940 Hz, and 1000 Hz. By generating a number of images throughout each vibration cycle, it is also possible to produce an animation of the organ oscillating. This is a powerful tool for observing potentially damaging oscillations. The first mode of oscillation follows the normal mode of deformation. It is normal for the gel layers to deform in shear as the otoconial layer is deflected roughly parallel to the sensory epithelium. Modes 2 and higher are not normal physiologic deformations. As seen in Figure 3.12, these modes are comprised of a combination of flexure and oscillation perpendicular to the plane of the organ.

### **Potential for Damage**

Previous studies have shown vestibular organ damage from exposure to intense sound (Ades, Graybiel, Morrill, Tolhurst, and Niven, 1958; Mangabeira-Albernaz, Covell, and Eldredge, 1959; McCabe and Lawrence, 1957). The modes of oscillation predicted by this model support these results. Significant oscillations perpendicular to the otolith layer may cause soft tissue damage in the weaker gel layers. Also, flexure of the otoconial layer may result in loss of otoconia. The natural frequencies calculated by this model support earlier research on low frequency sound damage to the vestibular organs. Previous human studies have shown high vestibular sensitivity to sounds of 1000 Hz and

less (Ades *et al.*, 1958). Animal studies have shown otolith trauma caused by similar frequencies (Mangabeira-Albernaz *et al.*, 1959).

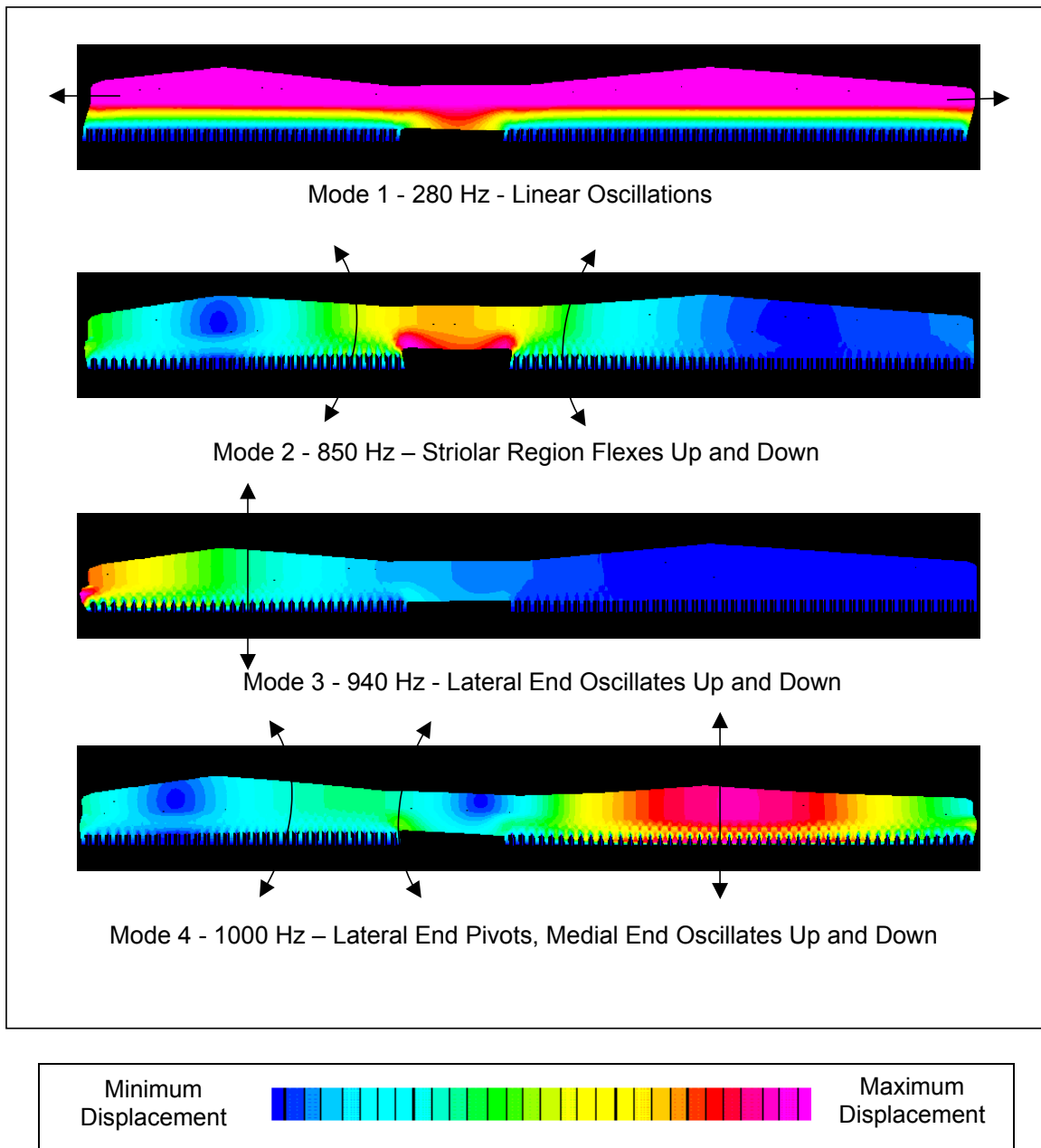


**Figure 3.12 – Results of the natural frequency analysis. The model is shown in its deformed state for the first four modes of oscillation.**

### 3.5 CONCLUSIONS

This modeling effort highlights the need for extensive anatomical experimentation to measure the material properties of the otolith organ. Accurate finite element model results depend upon detailed knowledge of the structure and physical properties of the item being modeled. This data set is incomplete for the otolith organs.

This model is a purely elastic two-dimensional representation of a generic mammalian otolith sensory macula. It does not include fluid damping or the added viscous damping that the presumed visco-elastic gel layer would contribute. This is not intended to be an exhaustive modeling study; it is rather a jumping-off point for more extensive three-dimensional modeling. Coupling such a 3-D model with an interactive computational fluid dynamics package would replicate the true kinematics of the organ. In spite of its limitations, the rather simple model presented here does bring to light some significant insights to otolith organ behavior.

- The model predicts hair cell cilia bundle deflection based on otolith organ deformation. Other finite element models exist that focus strictly on the hair bundle itself and how it deforms under a given load. This is the first finite element model that predicts otolith organ hair cell deflection as a result of a given load acting on the entire organ.

- A hair cell, with a given stiffness, can sense only a limited range of accelerations. The magnitude of this sensing range is less than the magnitude of the range of accelerations to which a mammal may be subjected. Variations in bundle stiffness result in extending the range of accelerations to which the organ can respond. Therefore, a range of bundle stiffnesses must exist within each organ.
- Natural frequencies predicted by the model are consistent with published accounts of low frequency sound damage to the otolith organ. Even though fluid damping has not been included in the calculation of these frequencies, the additional damping would primarily affect the amplitude of the vibrations, and only slightly affect the values of the natural frequencies.

## Chapter 4

# *An Underwater Video– Oculography System to Monitor Vestibular Output*

### **4.1 BACKGROUND**

During the course of their normal underwater duties, United States Navy Divers may be exposed to intense water-borne sound from sources such as sonar, underwater construction, or explosions. The effect of sound on the human in-water is still largely unknown. The Naval Submarine Medical Research Laboratory is involved in on-going research to determine sound effects on the human body in-water, including the effects on the vestibular apparatus and central nervous system. During a recent study, one diver exposed to 15 continuous minutes of a 240 Hz warble sound signal [an oscillating signal centered at 240Hz with  $\pm 80$  Hz bandwidth] at 160 dB re to 1  $\mu\text{Pa}$ <sup>1</sup>, and a second diver exposed to 15 continuous minutes of 1000 Hz at 181 dB, developed symptoms of lightheadedness, marked decrease in wakefulness, and an inability to concentrate. In both cases, symptoms apparently resolved within 30 minutes after sound exposure,

---

<sup>1</sup>Sound pressure levels in air are referenced to 20  $\mu\text{Pa}$ , while in water the reference is to 1  $\mu\text{Pa}$ . To convert, it is necessary to add 26 dB to the in-air intensity. e.g. - 100 dB re 20  $\mu\text{Pa}$  = 126 dB re 1  $\mu\text{Pa}$

however, both divers reported recurrent symptoms during the following weeks. An extensive medical workup suggested the vestibular apparatus and/or central nervous system as potentially responsible (Steevens *et al.*, 1999). It is the purpose of this present study to attempt to develop a method for quantifying the effects of intense underwater sound on the vestibular apparatus.

With the present state of the art, it is not possible to quantify vestibular function by making direct neural recordings from the human vestibular system. Therefore it is necessary to use other measures to study the performance of the vestibular apparatus. A quantitative measure of vestibular performance can be obtained by measurement of vestibular nystagmus (Baloh and Honrubia, 1990; Leigh and Zee, 1991). Vestibular nystagmus is reflexive rhythmic eye movements generated by the vestibular system when it is stimulated by head accelerations or other input.

When the head is subjected to an acceleration, the brain generates a compensatory eye movement. This is known as the vestibulo-ocular reflex or VOR. For a linear translation of the head, the eye movement relative to the skull is in a direction opposite to the direction of head translation (Paige and Tomko, 1991). During prolonged stimulation, rapid eye movements in the direction of the head translation also occur. These rapid eye movements, saccades, are anti-compensatory, and are necessary because the amount of angular displacement of the eye is limited. The saccades effectively reset the eye, returning it to a position such that the compensatory eye movements can continue (Boff and Lincoln, 1988).

Video recordings of eye movement during nystagmus provide a continuous quantitative measure of vestibular function that is relatively easy – as compared to neural recordings – to obtain and analyze. By recording eye velocity and detecting and removing the fast phase saccades from the eye velocity record, investigators are able to infer the net compensatory eye velocity command to the oculomotor system coming from the central vestibular system. This is indicative of the level of stimulation of the vestibular system.

Acceleration is not the only stimulus that can cause nystagmus. Sound induced vestibular stimulation has also been documented. There are many reported cases of vestibular symptoms in humans working in high-noise environments such as near aircraft engines or with firearms (Golz and Westerman, 2001; Oosterveld, Polman, and Schoonheydt, 1980). These are examples of broadband or impulse type sound sources. Of particular interest to the present study is the occurrence of low-frequency-sound vestibular stimulation. Ades, Graybiel, Morrill, Tolhurst, and Niven (1958) reported nystagmus in two deaf subjects with functioning vestibular systems when exposed to 151 dB re to 1  $\mu$ Pa, 250 Hz sound. They also reported a nystagmus at 146 dB re to 1  $\mu$ Pa, 590 Hz. Erlich and Lawson (1980) reported nystagmus at 136 dB re to 1  $\mu$ Pa, 500 Hz in 50 subjects. Kwee (1976), and Parker, Tubbs, and Littlefield (1978) reported nystagmus in subjects exposed to sound at frequencies of 500, 750, and 1000 Hz.

Sound induced vestibular stimulation in water is not as well studied. One study, with relevance to the current topic, was performed by Montague and Strickland (1961).

Divers were subjected to underwater sound in the range of 250 to 6000 Hz. The focus of this study was the auditory effect of the sound on the divers, in particular when the sounds were initially heard and when the subjects could no longer tolerate the sound. A by-product of the study, which is of interest here, was that extra-auditory symptoms, usually rotational movements of the visual field, were observed. These symptoms were reported for all subjects at 191 dB re 1  $\mu$ Pa, with increasing severity with greater signal intensity. Unfortunately, the particular frequencies at which this occurred, were not reported. All symptoms of movement stopped when the tone was terminated, with no residual effects. The authors suspected that these extra-auditory symptoms of visual field rotation could be attributed to vestibular stimulation.

In the present work, an underwater video-oculography (VOG) system was developed in an effort to quantify the effects of intense underwater sound on the vestibular apparatus. This system was used to monitor divers' eye movements during exposure to 160 dB, 200-300 Hz sound to determine if any vestibular stimulation occurred as a result of the sound.

## **4.2 MATERIALS AND METHODS**

### ***4.2.1 Equipment***

The underwater eye movement measurement system consisted of the following components; 1) an Outland Technologies underwater video camera with an infrared light source, 2) an Hewlit Packard dual AC to DC power supply, 3) an ISCAN RK-426



pupillary reflection eye tracking system, 4) a Sony Hi-8 VCR, and 5) an HEI module video data system. Infrared light, invisible to the human eye, is used to illuminate the eye in studies that monitor vestibular-induced eye movement so the testing can be performed in darkness. This is important because visual cues that may influence reflexive eye movements are repressed by eliminating the subject's visual field. The underwater camera was attached to the divers' mask over the right eye with an adjustable mounting bracket. Two different mask configurations were utilized. One consisted of a full-face mask, covering the eyes, nose, and mouth, held on by a flexible rubber hood arrangement with the diver's ears exposed to the water and is shown in Figure 4.1. The other rig tested was a hard helmet, fully enclosing the head, and is shown in Figure 4.2. Both masks were surface supplied with air and were equipped with microphones to allow the divers to communicate with the surface

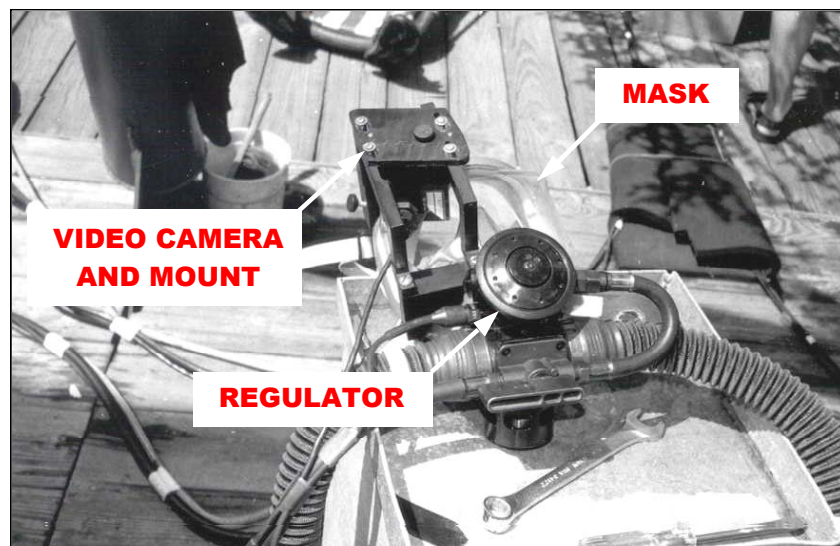


**Figure 4.1 – Full-face diving mask with video-oculography camera mounted over right eye.**

The camera mounting bracket on the soft hooded mask allowed translational adjustment along two axes, vertically to center the diver's eye in the video image, and horizontally,



**Figure 4.2 – Fully enclosed diving helmet with video-oculography camera mounted over right eye.**

along the line of sight, for camera focus. Camera position adjustment on the hard helmet was limited to the horizontal direction for camera focus. Waterproof cables attached to the divers' umbilical cable sent power to the camera and relayed the video image to a surface control room.

The divers were also fitted with electro-cardiogram (ECG) leads to monitor their heart rates during each dive. These analog signals were likewise sent via waterproof cable to the surface control room where they were observed by a Diving Medical Officer. Once received in the control room (Figure 4.3), the video signal from the underwater camera was routed through a video-Y connector. One path of the video signal was routed to an HEI module video data system. The HEI module put a bar coded time stamp on the

video signal. The output was then recorded on a SONY Hi8mm recorder. An Hi8 mm recorder was used due to its 400 line horizontal resolution format, which is necessary for post-experiment processing of the video data. Post processing of the eye movements was performed using the NASA-developed Video Ocular Movement System or VOMS (Sung and Reschke, 1997). VOMS digitizes the archived video signal and calculates the

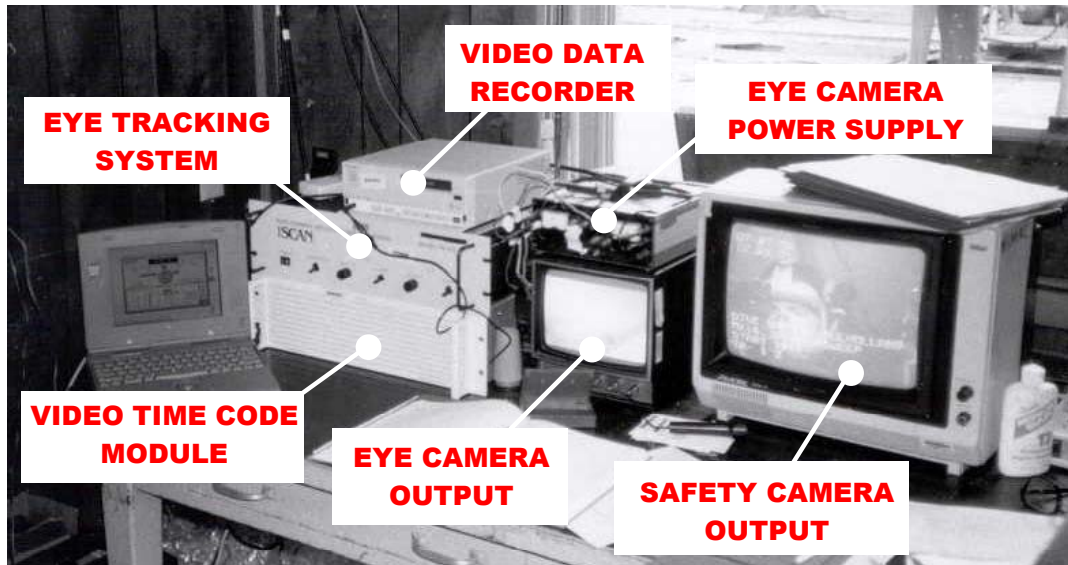
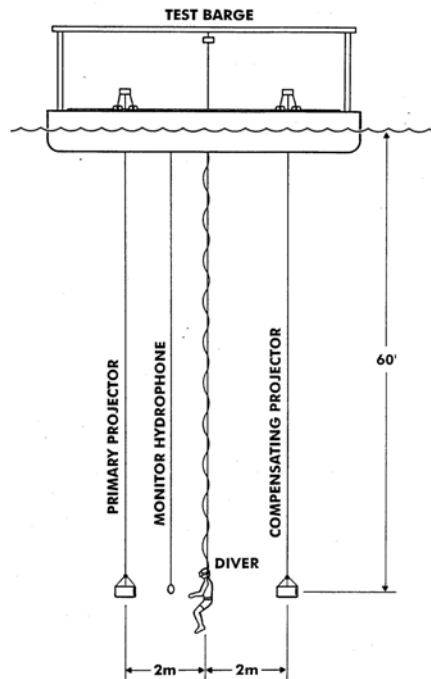


Figure 4.3 – Control room set-up.

horizontal, vertical and torsional eye movements. The other video path was routed to an ISCAN RK-426 Pupil/Corneal Reflection Tracking Unit. The ISCAN system has real-time image processing and evaluation capabilities that allowed the operator to verify that the quality of the video image was adequate. The ISCAN system provided real-time tracking of the horizontal and vertical movements of the eye. The ability to monitor these movements is a prerequisite for detecting torsional movements.

Two different sound signals were tested. One was a sweep tone of 230 to 320 Hertz and the second was a warble tone at 240 +/- 80 Hertz. Both signals were at a sound pressure

level of 160 dB re to 1  $\mu$ Pa. Sound exposures were 100 seconds in duration with a 50% duty cycle and a total of nine exposures per dive, resulting in 15 minutes daily cumulative exposure.



**Figure 4.4 – Sound field test set-up (from NSMRL, 1995).**

The sound source was a pre-recorded signal played on a digital audio tape recorder. This sound signal was split into two paths. Each path was filtered and amplified before one was sent to a source projector and the other was sent to a cancellation projector - both underwater. The projectors were separated by 400 cm with the diver centered between them facing the source projector. Extensive pre-dive sound mapping, both with and without a diver mannequin present, verified the uniformity of the sound field in the test area (NUWC 0597 & 0646, 1995). To monitor the sound during testing, a hydrophone was located 61 cm to the left of the diver at chest level (Figure 4.4). The output of the

hydrophone was monitored with a spectrum analyzer and was connected to a safety switch preset to kill the signal to the projectors if the sound pressure level in the test area exceeded 163 dB re 1  $\mu$ Pa.

#### ***4.2.2 Subjects***

Eight United States Navy divers, six experimental and two controls, served as subjects. The subjects were male, aged 22 to 34. All divers passed Navy fitness-to-dive physical examinations and underwent rigorous neurological and otological test batteries prior to the experiment. There were no signs of vestibular disorders in any of the subjects.



**Figure 4.5 – Subject wearing full-face mask with eye camera entering test area.**

#### **4.2.3 Procedure**

The test battery consisted of one day of diving at 30 feet and eight days of diving at 60 feet. All testing took place in open water. Each diver performed one dive per day. At the beginning and end of each diving day all divers were given an audiogram to monitor any threshold shifts in hearing throughout the experiment. Immediately before and after each sound exposure, rapid screening tests of the diver's neuro-otologic function were administered. These included dynamic posturography and dynamic visual acuity. The subject was then prepared to enter the water. ECG leads to monitor heart rate were applied beneath the wetsuit. The mask was put in place and camera position and focus were adjusted. When an acceptable video image was obtained the diver entered the water as seen in Figure 4.5. The diver descended to the test depth of either 30 or 60 feet and hooked into a sled positioned in the sound test area between the two sound projectors. The sled maintained the diver's position during the test and also served as a safety device; see Figure 4.6. The attitude of the diver's body was upright.

Once at depth, and prior to beginning the sound exposure, divers were cued to perform voluntary head tilts to produce torsional eye movements. These torsional movements were recorded for post-dive analysis to verify that the data analysis system had the capability of detecting torsion from the underwater video image.

VOG was only a part of the study. Divers were also required to perform a sustained attention task during sound exposure. Their performance was monitored to see if the

sound had any detrimental effects on their cognitive abilities. Surface personnel interviewed the diver during sound exposure to determine if the diver was experiencing any physical symptoms due to the sound.

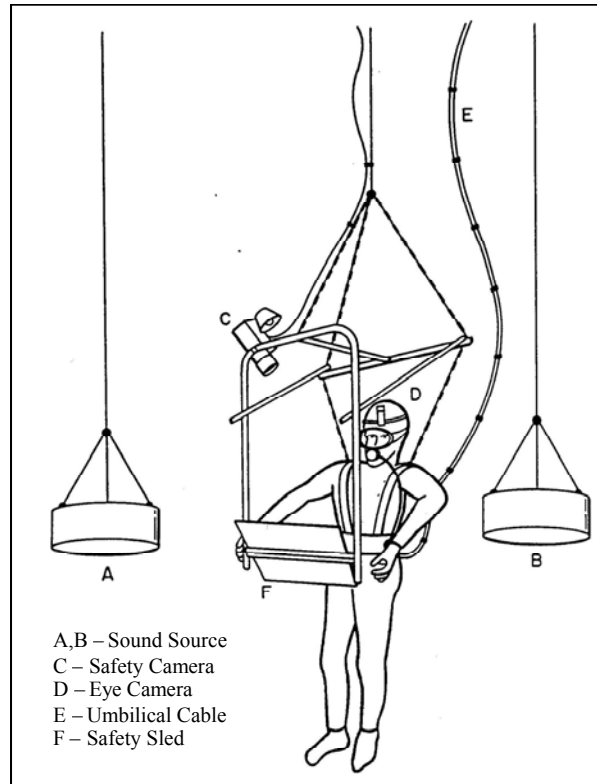


**Figure 4. 6 – Diver in test position (from NSMRL, 1995)**

The sequence of events during each dive was as follows. The diver entered the water and descended to the test depth. Incandescent light illuminated the test area. Video recording and real time monitoring of the eye image began. Once the diver was in place, the video image was checked and the diver was notified of necessary camera adjustments. When an acceptable image was achieved the diver was cued to make a series of head tilts. That is, looking straight ahead, the diver dropped his right ear to his shoulder then brought his head straight up to a normal position. The diver then dropped his left ear to his shoulder

and again brought it back to a normal position. The right and left tilts were then repeated. These head movements caused a reflexive, compensatory, torsional movement of the eyeballs, which was recorded. After this calibration procedure was completed, the sound exposure began. The sound was turned on for 100 seconds. With the incandescent light still on, the diver began the sustained attention task. The diver was also simultaneously interviewed. When the task and interview were complete, approximately 50 seconds into the sound exposure, the incandescent light was turned off and the diver was cued to remain still and gaze straight ahead. This was the dedicated VOG portion of the sound exposure. Real time monitoring, by the surface operator, for any positional nystagmus, occurred for the duration of the sound exposure. At the end of the 100-second exposure, the sound was turned off, the incandescent light was turned on, and the diver was allowed to rest for 100 seconds. This cycle, of 100 seconds sound on 100 seconds sound off, was repeated nine times for a total of 15 minutes cumulative sound exposure. The diver then returned to the surface for post-exposure testing.

### **4.3 RESULTS**

During each 100-second underwater sound exposure, eye movements were analyzed for the latter 50 seconds of the exposure. An operator at the surface, using the ISCAN pupillary reflection tracking system to process the video signal, looked for real-time nystagmus. No spontaneous primary position nystagmus, vertical or horizontal, was detected in any diver in any test. The operator also qualitatively observed the raw video image for torsional nystagmus. None was detected.



When testing was complete, the recorded video data was analyzed for torsional nystagmus. The NASA-developed VOMS system was used for this purpose. The bar-coded tape times, corresponding to the head tilt portion of the dive and the 50 second dedicated VOG portions of the sound exposures, were entered into the program for batch processing. A scanner digitized the video images during these defined time periods. On each frame, the center and diameter of the pupil was identified. A series of concentric rings was then drawn from the outer edge of the pupil to the outer edge of the iris as shown in Figure 4.7. The pixel pattern under each ring, which corresponded to the subtleties in shading of the subject's iris, was recorded. The pixel pattern under each ring in the subsequent frame was compared to the pattern in the previous frame. Any rotational shift in the pixel pattern, and hence any torsional movement of the eye, could be tracked in this manner.

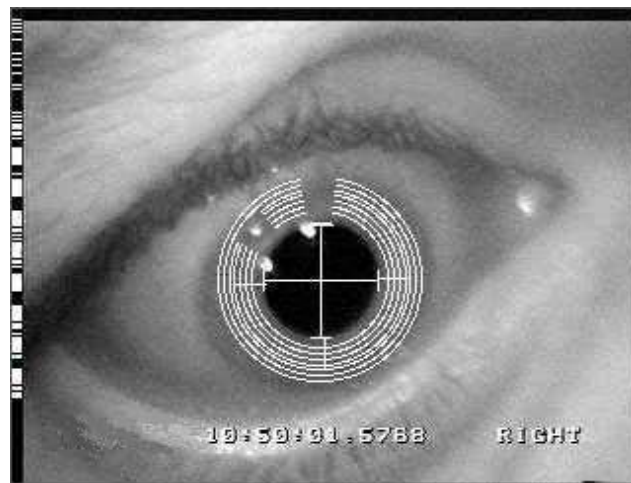


**Figure 4.7 – Digitized eye image during torsional nystagmus analysis.**

Some sample data is presented in Figures 4.8 and 4.9. Figure 4.8 shows the torsional eye movement that occurred when the diver was cued to tilt his head at the start of the dive as

previously described. The zero shifts between tilts are a result of the subject not returning his head to precisely the original upright position. The head tilts produced torsion angles ranging from approximately 7 to 11 degrees of rotation. This data verifies that the VOG system developed for this study is capable of producing underwater video image of quality sufficient for torsional analysis.

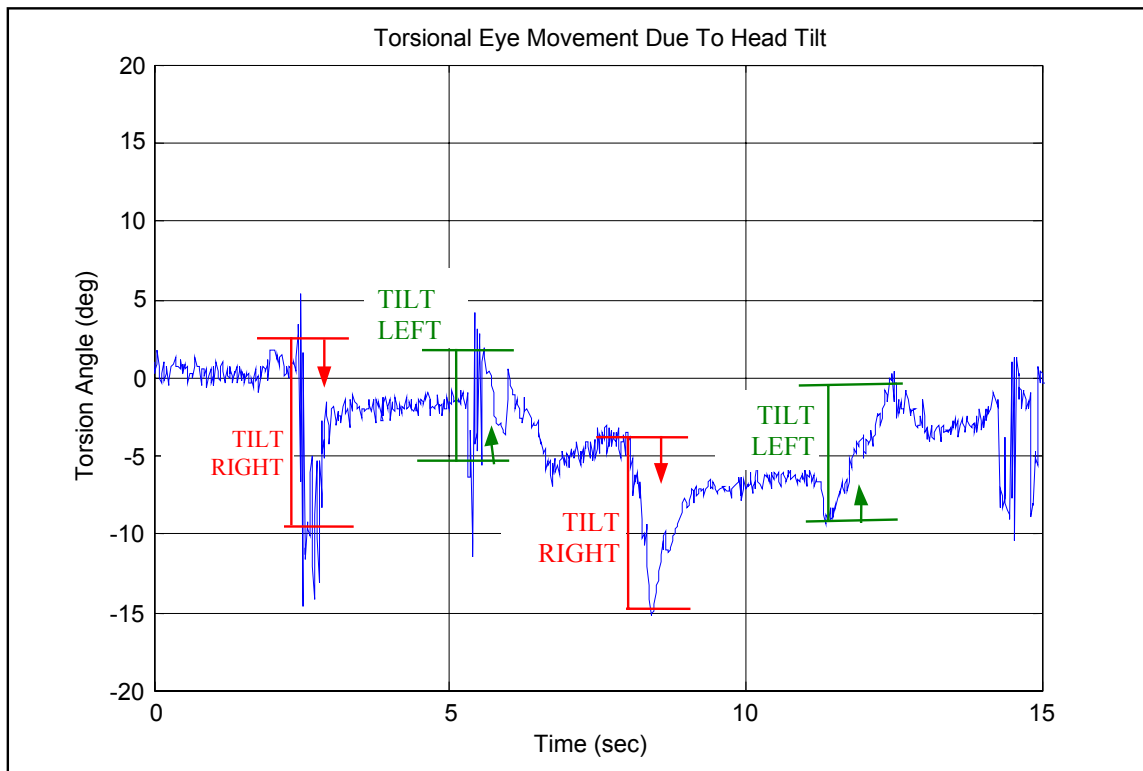


**Figure 4.8 – Graph of eye torsion angle versus time during the head tilt portion of the dive.**

Figure 4.9 presents data analyzed during a sound exposure. The signal is noisier because the video image quality had degraded somewhat from the start of the dive (when the head tilts were performed). As each dive progressed, the eye position relative to the camera

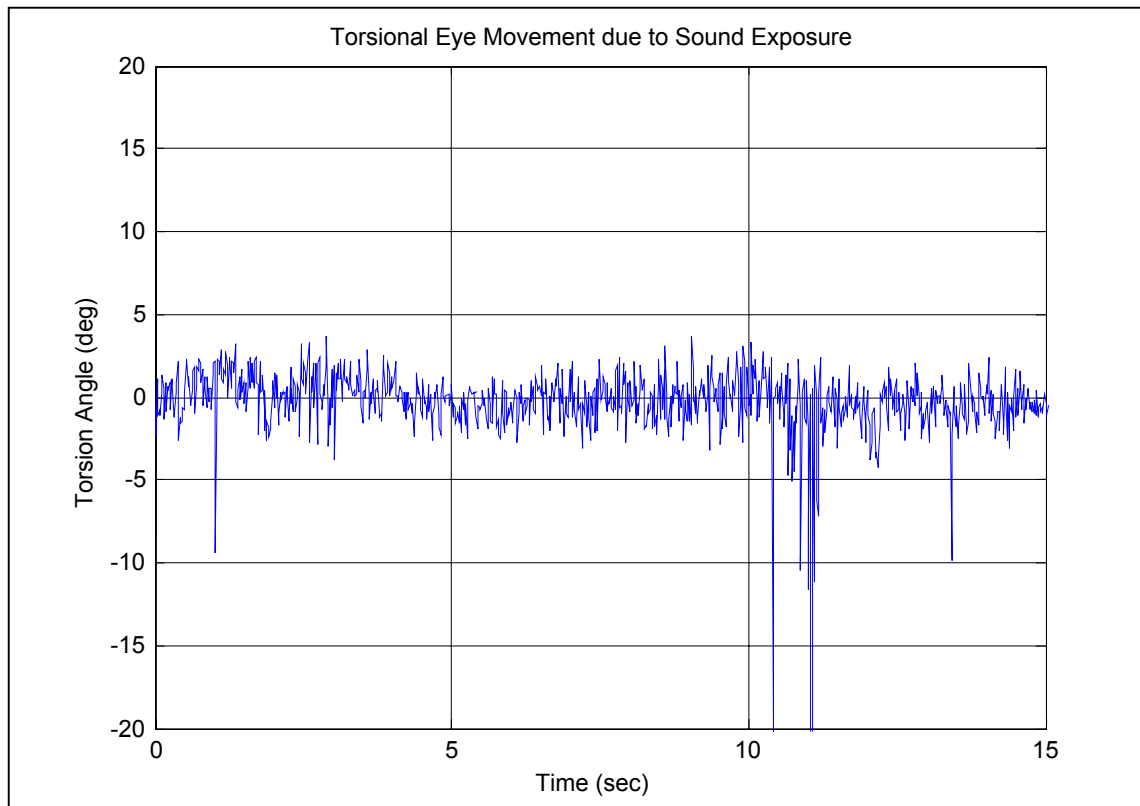


**Figure 4.9 – Graph of eye torsion angle versus time during the sound exposure portion of the dive**

inevitably changed causing a decrease in focus quality. Slight fluctuations of the data mean about zero can be noted and are due to the fact that the diver's head was not completely immobile. Slight tilts of the head result in slight torsional movements of the eyes. These low-frequency eye movements are distinguishable from torsional nystagmus as nystagmus has distinct slow and fast phases at a higher frequency resulting in a saw-tooth data pattern. The subject blinking causes the large negative spikes in the data. The data sample presented here was typical.

## 4.4 DISCUSSION

This experiment proved successful in producing and recording underwater video eye images for nystagmus analysis. No horizontal, vertical, or torsional nystagmus was detected in any diver either during real-time data analysis or during post-experiment data processing. In this study, the ambient light level at both 30 and 60 feet, although dim, was sufficient to allow divers to view their surroundings. These visual references may have suppressed vestibular response. Traditionally, VOG studies are performed in total darkness in an attempt to isolate the vestibular response. Future underwater sound exposure studies should take this into account. Furthermore, previous studies mentioned in this text that resulted in sound-induced eye movements used continuous sound exposure as a stimulus. The 50% duty cycle tested in this study may have inhibited sound-induced vestibular stimulation and hence eye movements generated by the vestibular system.

Several features of the experimental process could benefit from being refined. Perhaps the most fundamental problem to be addressed is the limited ability to focus the camera due to mount design. Due to natural variations in human skull shapes, each diver's eye is a different distance from the window of the mask. This makes adjustment in the horizontal direction, along the line of sight, critical to obtain good focus. The amount of travel built into the camera mount in the line-of-sight direction was in some cases inadequate to make good focus possible. Compounding the problem, the flexibility of the full-face mask caused variations in camera focus. Field solution was to have the diver

hold the mask snugly against his face at the surface for focusing, and again during the VOG portion of the sound exposure.

Ease of adjustment of camera focus is also an area requiring improvement. Focus of the camera was initially adjusted at the surface. Once the diver entered the water, the ambient pressure would cause his equipment to shift relative to his body, including both soft and hard diving helmets. In some cases this would be enough to make refocusing necessary. The focus adjustments on the existing camera mounts were very difficult for a gloved diver to manipulate when cued to do so by the surface operator. Any new design should take this into account and include focus adjustment that has a positive feel, is easily operated by a subject wearing gloves, and can be locked in place once properly adjusted. An alternative would be remote camera focusing operated by surface personnel.

The camera was mounted directly in front of the diver's right eye thus blocking his visual field for task performance. In traditional VOG studies cameras are mounted off-axis from the eyes and infrared mirrors reflect the eye image into the camera. These dichroic mirrors are transparent to incandescent light, so the subject's vision is not obstructed. If this technology is feasible for an underwater application, it should be incorporated in future studies where task performance is required of the subjects.

Bubbles, when the diver exhaled, would travel into his visual field giving a visual reference. Since the vestibular system is so closely tied to the oculomotor system, visual

cues can affect and inhibit vestibular stimulation. In this case the direction of travel of the bubbles rising to the surface was sufficient to orient the diver and perhaps suppress conflicting vestibular output. Another problem was that some bubbles would lodge on the camera lens distorting the video image. Field solution was to install a bubble deflector over the regulator exhaust port.

## **4.5 CONCLUSIONS**

Eight United States Navy divers were exposed to 15 minutes daily cumulative underwater low-frequency sound at 160 dB re 1  $\mu$ Pa. They were fitted with an underwater video camera that relayed an image of their right eye to the surface. The image was analyzed both real-time and post-experiment for vestibular induced nystagmus. No nystagmus, horizontal, vertical or torsional, was detected in any divers during the underwater sound exposures. The divers' performance of a sustained attention task during the sound exposures was also monitored. This experiment was the first successful attempt to record and analyze eye movements in the underwater environment.

## *Chapter 5*

### *Concluding Remarks*

The United States Navy views the vestibular system as a potential target for non-lethal weapon systems. Incapacitating symptoms previously suffered by Navy divers, attributed to the vestibular system, have been a motivating force for this endeavor. A thorough understanding of, and the ability to predict the function/response of, the vestibular system is necessary to make this weapon system a reality, and to protect friendly personnel from similar weapons. Modeling of the vestibular organs both analytically and using finite element methods is crucial to gain an in-depth understanding of their function. Only when a complete understanding of the organ system is achieved will engineers be able to design effective non-lethal weapons targeting this system. In the design and development of these weapon systems, monitoring the output of the vestibular system will be necessary to determine the effectiveness of the weapon and also for calibration purposes. Since a likely application for the vestibular-based non-lethal weapon will be in an underwater scenario against unfriendly diving personnel, the ability to monitor vestibular output in that realm is mandatory. This dissertation has presented two vestibular modeling approaches, and has discussed the development of an underwater video-oculography system for use in monitoring vestibular output.

The first modeling approach presented here has produced a simplified mechanical transfer function that yields analytic time domain solutions for otoconial layer displacement. These simplified time domain solutions have proven to be a good approximation for the full finite difference solution to the original partial differential equation set developed in previous work. The derivation of the simplified TF is purely theoretical, however, its results correlate well with experimental frequency response data.

The time constants calculated from the simplified TF indicate that the dynamic response of the otolithic organs is extremely fast. The mechanotransduction process has a long time constant, which may range from 0.004 to 0.2 sec, and a short time constant in the 0.02 to 0.4 msec range. These time constants signify that the mechanical response to acceleration inputs and gravity direction changes during head tilt is extremely rapid. With such a fast mechanical response, acceleration stimuli rapidly produce deflections of the otoconial layer that are proportional to the acceleration. For any second-order over damped system to function as an accelerometer, it must have short time constants to have adequate dynamic response. It should, therefore, come as no surprise that the otoliths have such short time constants. The frequency response match, of the simplified mechanical TF to physiologic data from first-order neuron recordings, indicates that the mechanoelectrical transduction and neural response are equally fast. Thus acceleration and gravity information is rapidly reported to the vestibular nuclei of the central nervous system. Such rapid response is probably required for normal animal locomotion on the earth.



The approximate dynamic transfer function developed here is the only lumped parameter model available that quantitatively describes utricle and saccule mechanical dynamic function. This model has its origins in a more complex distributed parameter model but is simplified to an easily usable form that yields results comparable to the more complex model. This simplified model may potentially be used to assess, in real-time, the effects of non-lethal weapons on the otolith system. Additional uses of the model include developing clinical otolith function tests and developing experiments to test central nervous system response to otolith acceleration inputs.

The second modeling approach is a purely elastic two-dimensional finite element representation of a generic mammalian otolith sensory macula. It does not include fluid damping or the added viscous damping that the presumed visco-elastic gel layer would contribute. This is not intended to be an exhaustive modeling study; it is rather a jumping-off point for more extensive three-dimensional modeling. Coupling such a 3-D model with an interactive computational fluid dynamics package would replicate the true kinematics of the organ. In spite of its limitations, the rather simple model presented here does bring to light some significant insights to otolith organ behavior.

The model predicts hair cell cilia bundle deflection based on otolith organ deformation. Other finite element models exist that focus strictly on the hair bundle itself and how it deforms under a given load (Duncan and Grant, 1997; Cotton and Grant, 2000). This is the first finite element model that predicts otolith organ hair cell deflection as a result of a given load acting on the entire organ. A hair cell, with a given stiffness, can sense only a

limited range of accelerations. The magnitude of this sensing range is less than the magnitude of the range of accelerations to which a mammal may be subjected. Variations in bundle stiffness result in extending the range of accelerations to which the organ can respond. Therefore, this finite element model supports the hypothesis that a range of bundle stiffnesses must exist within each organ.

Natural frequencies predicted by the model are consistent with published accounts of low frequency sound damage to the otolith organ. Even though fluid damping has not been included in the calculation of these frequencies, the additional damping would only affect the amplitude of the vibrations, not the values of the natural frequencies.

Finally, an approach to monitor vestibular function in the underwater environment was developed. Eight United States Navy divers were exposed to 15 minutes daily cumulative underwater low-frequency sound at 160 dB re 1  $\mu$ Pa. They were fitted with an underwater video camera that relayed an image of their right eye to the surface. The image was analyzed both real-time and post-experiment for vestibular induced nystagmus. No nystagmus, horizontal, vertical or torsional, was detected in any divers during the underwater sound exposures. The divers' performance of a sustained attention task during the sound exposures was also monitored. This experiment was the first successful attempt to record and analyze eye movements in the underwater environment.

## REFERENCES

- Ades HW, Graybiel A, Morrill SN, Tolhurst GC, Niven JL. (1958). Non-auditory effects of high intensity sound stimulation on deaf human subjects. Defense Technical Information Center, Technical Report No. AD-208011.
- Almaz Optics, Inc. (2001). Calcium Carbonate (CALCITE),  $\text{CaCO}_3$ .  
<http://www.almazoptics.com/homepage/CaCO3.htm>.
- Ashmore JF. (1983). The stiffness of the sensory hair bundle of frog saccular hair cells. *Nature*, Lond. 304:536-538.
- Baloh RW, Honrubia V. (1990). Clinical Neurophysiology of the Vestibular System, ed 2. FA Davis, Philadelphia.
- Barrett MD. (1995). A fiber optic interferometer for measuring submicrometer displacements of ciliary bundles, Virginia Tech Thesis.
- Barrett MD, Peterson EH, Grant JW. (1999). Extrinsic Fabry-Perot interferometer for measuring the stiffness of ciliary bundles on hair cells. *IEEE Trans Biomed Eng*, Vol. 46:331-339.
- Bedard, ER. (2000). Joint Non-Lethal Weapons Program (JNLWP) Master Plan. (Internet) [http://www.jnlwd.usmc.mil/Documents/master\\_plan.pdf](http://www.jnlwd.usmc.mil/Documents/master_plan.pdf). Quantico, Virginia: Joint Non-Lethal Weapons Directorate.

Benser ME, Issa NP, Hudspeth AJ. (1993). Hair-bundle stiffness dominates the elastic reactance to otolithic-membrane shear. *Hearing Res.*, 68:243-252.

Benson AJ. (1999). Spatial disorientation – common illusions. In J Ernsting, AN Nicholson, KJ Rainford (Eds.), *Aviation medicine*, (3<sup>rd</sup> ed., pp.437-481), Oxford: Butterworth Heinemann.

Boff KR, Lincoln JE. (1988). Engineering Data Compendium: Human Perception and Performance. AAMRL, Wright-Patterson AFB, OH.

Carlstrom D. (1963). A crystallographic study of vertebrate otoliths. *Biol. Bull.*, 125:441-463.

Cook R, Malkus D, and Plesha M. (1989). Concepts and Applications of Finite Element Analysis 3<sup>rd</sup> Edition, John Wiley & Sons, New York, NY.

Cotton JR, Grant JW. (2000). A finite element method for mechanical response of hair cell ciliary bundles. *J. Biomech. Eng.*, 122:44-50.

Curthoys IS, Oman CM. (1987). Dimensions of the horizontal semicircular duct, ampulla and utricle in the human. *Acta Otolaryngol*, 103:254-261.

Curthoys IS. (1996). Personal communication. Sydney University, Department of Psychology, Sydney, Australia.

Denise P, C Darlot, J Droulez, B Cohen, A Berthoz. (1988). Motion perceptions induced by off-vertical axis rotation (OVAR) at small angles of tilt. *Exp. Brain Res.* 73:106-114.

Denk W, Webb WW, Hudspeth AJ. (1989). Mechanical properties of sensory hair bundles are reflected in their Brownian motion measured with a laser differential interferometer. *Proceedings of the National Academy of Science USA*, 86:5371-5375.

Duncan RK, Grant JW. (1997). A finite element model of inner ear hair bundle micromechanics. *Hearing Res.*, 104:15-26.

Erlich MA, Lawson W. (1980). The incidence and significance of the Tullio phenomenon in man. *Otolaryngol Head Neck Surg* 88:630-635 (Sept-Oct).

Fernandez C, Goldberg JM, Baird RA. (1990). The vestibular nerve of the chinchilla III. *J. Neurophysiology*, 63:767-804.

Ferreira EA, Grant JW, Peterson EH. (1996). Finite element model for analysis of otolithic membrane and ciliary bundle deformation, *Assoc. Res. Otolaryngol. Abs.*:76.

Gilbertson LG, Goel VK, Kong WZ, Clausen JD. (1995). Finite element methods in spine biomechanics research. *Crit Rev Biomed Eng.*;23(5-6):411-73. Review.

Gillingham KK, Previc FH. (1996). Spatial orientation in flight. In RL DeHart (Ed.), *Fundamentals of aerospace medicine*. (2<sup>nd</sup> ed., pp. 309-398). Lea & Febiger, Philadelphia, PA.

Goldberg JM, G Desmadryl, RA Baird, C Fernandez. (1990). The vestibular nerve of the chinchilla IV. Discharge properties of the utricular afferents. *J. Neurophysio.* 63:781-90.

Golz A, Westerman ST, *et al.* (2001). The effects of noise on the vestibular system. *American Journal of Otolaryngology*, 22(3):190-196.

Grant JW, CC Huang, JR Cotton. (1994). Theoretical mechanical frequency response of the otolithic organs. *J. Vestibular Res.* 4:137-51.

Grant JW, JR Cotton. (1990/91). A model for otolith dynamic response with viscoelastic gel layer. *J. Vestibular Res.* 1:139-51.

Grant JW, WA Best, R LoNigro. (1984). Governing equations of motion for the otolith organs and their response to a step change in velocity of the skull. *J. Biomechanical Eng.* 106:302-8.

Grant W, Best W. (1987). Otolith-organ mechanics: Lumped parameter model and dynamic response. *Aviation, Space and Environmental Medicine*, October, 970-976.

Henson OW, et al. (2000), [http://www-cellbio.med.unc.edu/henson\\_mrm](http://www-cellbio.med.unc.edu/henson_mrm),  
Department of Cell and Developmental Biology, University of North Carolina,  
Chapel Hill and The Center for In Vivo Microscopy, Duke University, Durham, NC,  
Copyright 2000.

Howard J, Ashmore JF. (1986). Stiffness of sensory hair bundles in the sacculus of the frog. *Hearing Res.* 23:93-104.

Howard J, Hudspeth AJ. (1988). Compliance of the hair bundle associated with gating of mechano-electrical transduction channels in the bullfrog's saccular hair cell. *Neuron*, 1:189-199.

Hudetz WJ. (1973). A computer simulation of the otolith membrane. *Computat. Biol. Med.* 3:355-69.

Hudspeth AJ. (1989). *Nature*. Vol. 341.

Hughes CA, McGrath BJ, McGrath EA, Rupert AH. (2001). Finite element model of the cupula, *Assoc. Res. Otolaryngol. Abs.*:21303.

Huiskes R, Chao EY. (1983). A survey of finite element analysis in orthopedic biomechanics: the first decade. *J Biomech*, 16(6):385-409. Review.

Igarashi M. (1966) Dimensional study of the vestibular end organ apparatus. 2<sup>nd</sup> Symposium on the role of the vestibular organs in space exploration. NASA SP-115.

- Jongkees LBW. (1967). On the otoliths: Their function and the way to test them. 3<sup>rd</sup> Symposium on the role of the vestibular organs in space exploration. NASA SP-152.
- Kachar B, Parakkal M, Fex J. (1990). Structural basis for mechanical transduction in the frog vestibular sensory apparatus: I. The otolithic membrane. *Hearing Res.* 45:179-90.
- Kelly JP. (1991). The sense of balance. Principles of Neural Science 3<sup>rd</sup> Edition. Appleton and Lange, Norwalk, CT.
- Kondrachuk AV, IY Schehechkin, SP Sirenko. (1986). Structure and function of otoliths. *Kosmicheskaya Biol.* 6:60-70.
- Kondrachuk AV. (2000). Computer simulation of the mechanical stimulation of the saccular membrane of bullfrog. *Hearing Res.*, 143:130-138.
- Kondrachuk AV. (2001). Finite element modeling of the 3D otolith structure, *J. Vestib. Res.*, 11:13-32.
- Kwee HL. (1976). The occurrence of the Tullio phenomenon in congenitally deaf children, *The Journal of Laryngology and Otology*, June.
- Leigh JR, Zee DS. (1991). The neurology of eye movements, ed 2. FA Davis, Philadelphia, PA.



Lindeman HH, Ades HW, West RW. (1970). Scanning electron microscopy of the vestibular end organs. 5<sup>th</sup> Symposium on the role of the vestibular organs in space exploration. NASA SP-314, 145-156.

Lowenstein O, Roberts TDM. (1950). The equilibrium of the otolith organs of the thornback ray. *J. Physiol.*, 110:392-415.

Mangabeira-Albernaz PL, Covell WP, Eldredge DH. (1959). Changes in the vestibular labyrinth with intense sound. *Laryngoscope*, 69:1478-1493.

McCabe BF, Lawrence M. (1957). The effects of intense sound on the non-auditory labyrinth. *Acta Otolaryngol.* 49:147-157.

Montague WE, Strickland JF. (1961). Sensitivity of the water-immersed ear to high- and low-level tones, *J. Acoust. Soc. Am.* 33(10).

Naval Submarine Medical Research Laboratory. (1995). Underwater Sound Conference Proceedings, Groton CT.

Naval Undersea Warfare Center, Leesburg Facility. (1995). Underwater Sound Reference Detachment Calibration Memorandum No. 0597.

Naval Undersea Warfare Center, Leesburg Facility. (1995). Underwater Sound Reference Detachment Calibration Memorandum No. 0646.

- Njeugna E, Eichorn J-L, Kopp C, Harlicot P. (1992). Mechanics of the cupula: effects of its thickness. *J. of Vestibular Research*, 2:227-234.
- Ohmori H. (1987). Gating properties of the mechano-electrical transducer channel in the dissociated vestibular hair cell of the chick, *J. Physiol* 387:589-609.
- Oosterveld WJ, Polman AR, Schoonheydt J. (1980). Noise-induced hearing loss and vestibular dysfunction. *Aviation, Space, and Environmental Medicine*, August.
- Paige GD, Tomko DL. (1991). Eye movement responses to linear head motion in the squirrel monkey. *Journal of Neurophysiology*, May, 65(5)1170-1182.
- Paige GD. (1994). Senescence of human visual-vestibular interactions: smooth pursuit, optokinetic, and vestibular control of eye movements with aging. *Exp. Brain Res.* 98:355-72.
- Park HK, Dujovny M, Park T, Diaz FG. (2001). Application of finite element analysis in neurosurgery. *Childs Nerv Syst*, 17(1-2):87-96. Review.
- Parker DE, Tubbs RL, Littlefield VM. (1978). Visual-field displacements in human beings evoked by acoustical transients, *J. Acoust. Soc. Am.* 63(6).
- Peterson EH. (1996). Personal correspondence. Ohio University, College of Osteopathic Medicine, Athens, OH.

Purificato, R. (2001). Center for non-lethal weapon research open at Brooks.

(Internet) <http://extra.afrl.af.mil/news/june01/>. San Antonio, Texas: Air Force Research Laboratory.

Reddy JN. (1993). An Introduction to the Finite Element Method, 2<sup>nd</sup> Edition, McGraw-Hill, Inc., New York, NY.

Spoendlin HH. (1965). Ultrastructural studies of the labyrinth in squirrel monkeys. The role of the vestibular organs in the exploration of space. NASA SP-77.

Steevens CC, Russell KL, Knafelc ME, Smith PF, Hopkins EW, Clark JB. (1999). Noise-induced neurologic disturbances in divers exposed to intense water-borne sound: two case reports. *Undersea Hyper. Med.*, 26(4): 261-5.

Strelioff and Flock A. (1984). Stiffness of sensory-cell hair bundles in the isolated guinea pig cochlea. *Hearing Res.* 15:19-28.

Sung K, Reschke MF. (1997). A model-based approach for the measurement of eye movements using image processing. NASA Technical Paper No. 3680.

Twizell EH, Curran DAS. (1977). A finite element model of the otolith membrane. *Comput. Biol. Med.*, 7:131-141.

Watanuki K, Schuknecht HF. (1976). A morphological study of human vestibular sensory epithelia. *Arch Otolaryngol*, 102:583-588.

Wilson VJ, Melvill Jones G. (1979). *Mammalian Vestibular Physiology*, Plenum Press, New York, NY.

Yin FC. (1985). Applications of the finite-element method to ventricular mechanics. *Crit Rev Biomed Eng*, 12(4):311-42. Review.

Young LR, Meiry JL. (1968). A revised dynamic otolith model. *Aerospace Medicine*, Vol. 39(6)605-608.

## **VITA**

Elizabeth Ferreira McGrath received a Bachelor of Science degree in Mechanical Engineering from the Southeastern Massachusetts University in Dartmouth, Massachusetts. This was followed by a Master of Science degree in the same field from the Massachusetts Institute of Technology in Cambridge, Massachusetts. While at MIT, Elizabeth performed research at the Sloan Automotive Laboratory concerning the flames in internal combustion engines. This led to a position as a development engineer with internal combustion engine manufacturer Outboard Marine Corporation at their test facility in southern Florida.

Having had enough fun in the sun, Elizabeth decided to return to academia at Virginia Tech and pursue a doctoral degree, this time with a research emphasis on biomedical engineering. She traveled to the Naval Aerospace Medical Research Laboratory in Pensacola, Florida where the research for this dissertation was performed and where she is currently employed as a research engineer.